We are IntechOpen, the world's leading publisher of Open Access books Built by scientists, for scientists

6,900
Open access books available

185,000
International authors and editors

200M
Downloads

Our authors are among the

154
Countries delivered to

TOP 1%
most cited scientists

12.2%
Contributors from top 500 universities



WEB OF SCIENCE™

Selection of our books indexed in the Book Citation Index in Web of Science™ Core Collection (BKCI)

Interested in publishing with us?
Contact book.department@intechopen.com

Numbers displayed above are based on latest data collected.
For more information visit www.intechopen.com



Chapter 2

Spark Plasma Sintering of Ultrafine WC Powders: A Combined Kinetic and Microstructural Study

A.K. Nanda Kumar and Kazuya Kurokawa

Additional information is available at the end of the chapter

http://dx.doi.org/10.5772/55291

1. Introduction

Nano grained cemented tungsten carbide (*n*-WC) is currently being researched for many potential applications in manufacturing processes. An example is the near net shape manufacturing of aspheric glass lenses. With the advent of optical technology and electro-optic systems, conventional spherical lenses are now being replaced by aspheric lenses of smaller dimensions and lower curvatures to be accommodated inside flat cellular phones and DVD readers. A cost effective method of fabricating such small aspheric lenses is by molding the glass gob in a suitable preform or mold at temperatures near the glass transition temperature (T_g). WC-based cemented carbides are a natural choice for the mold because of their high hot hardness and low coefficient of thermal expansion, CTE (which is compliant with the CTE of glass). A major issue in this near net shape fabrication method is that the surface finish of the carbide mold should be extremely smooth as otherwise the glass component will also reproduce the surface roughness of the mold. This eventually leads to aberration of the lens and a loss of precision, consequently necessitating the need for an extra grinding or polishing step after the manufacturing process. Ultra-fine grained carbides, owing to their small grain size, can be polished to extreme smoothness of the order of 2-3 nm or lesser. To facilitate the lens' release from the mold, usually Ir or Re coatings are applied on the mold surface. Generally, this arrangement works well for near net shape mass production of small aspheric lenses and is commonly used in lens manufacturing industries. Another instance where *n*-WC assumes commercial importance is in the micromachining industry where often extremely small holes have to be drilled into hard substrates. The drill-bit in such applications is made of WC with a very small curvature at its tip which is possible only if the grain size is in the nano-metric range. Larger grains lead to blunting when the tip undergoes brittle intergranular fracture resulting in chipping off a large chunk of the material from the drill tip.

INTECH
open science | open minds

© 2012 Kumar and Kurokawa, licensee InTech. This is an open access chapter distributed under the terms of the Creative Commons Attribution License (http://creativecommons.org/licenses/by/3.0), which permits unrestricted use, distribution, and reproduction in any medium, provided the original work is properly cited.

Given that cemented *n*-WC has many such industrial applications particularly owing to its mechanical strength, the microstructure, porosity (density) and grain size inarguably are of extreme significance in tailoring its properties like hardness, toughness and chemical stability. Powder metallurgical processes like Hot Iso-static Pressing (HIP) and high temperature solid state or liquid phase sintering are the usually employed methods of fabricating dense compacts of pure or cemented WC. However, pure WC in the absence of a binder is rather difficult to consolidate completely. While in cemented WC, the liquid phase assists sintering by particle rearrangement, the low diffusivities of W and C under pure solid state sintering conditions retard quick consolidation during sintering or HIP of pure n-WC. Therefore, unnaturally long durations (in the case of isothermal sintering) or very high temperatures in excess of 2000 C (in the case of non- isothermal sintering) are required for consolidation of n-WC. This disadvantage has led researchers to seek alternate or improvised sintering methods [Bartha L *et al*, 2000, Agrawal D *et al*, 2000, Breval E *et al*, 2005, Kim H C *et al*, 2004] like Spark Plasma Sintering (SPS) or microwave sintering to achieve quicker densification at lower time costs. The SPS method, in particular has attracted wide attention owing to its consistently good record of achieving the desired density at surprisingly low times and lower temperatures. The generation of very high current densities leading to a sort of, 'plasma welding' between the particles is suspected to be the chief cause of such a profit in the total energy budget compared to conventional sintering. However, no clear evidence exists for the actual generation of plasma or any surface melting phenomenon in the SPS process although the hypothesis has been widely debated [Tokita M, 1997, Hulbert D M *et al*, 2008, Hulbert D M *et al*, 2009].

Since the last decade, a number of reports on SPS of *n*-WC have consistently come up in journals and scientific magazines. Not only have the compacts been manufactured to complete density, but the grain size could also be limited to the ultra-fine size (200-400 nm). Usually Hall-Petch hardening is observed at low grain sizes and low cobalt content. This increased capability to constrain the microstructure to the ultrafine regime has been largely aided in part because of the commercial availability of nano powders of WC synthesized by many chemical routes and also partly because of the current popularity of activated sintering instruments that also accommodate high heating rates and pressure along with the presence of electromagnetic fields.

2. Activated sintering processes

Sintering methods involving the presence of an electric field are generally called Field Assisted Sintering Techniques (FASTs). Unlike conventional sintering - in which the sample is heated from the outside (furnace) - in FAST, the sample is heated internally by the passage of an electric current. Compared to the hot pressing process, FAST methods can have extremely high heating rates, sometimes even upto 2000 K/min [Tokita M *et al*, 2007, Cramer G D, 1944 and a host of other patents, a review of which can be found in the paper by Salvatore Grasso *et al*, 2009]. This is achieved by using current pulses from a few micro seconds to milli seconds but charged with an extremely high current density of about 10,000 A/cm^3. External pressures can also be applied from a few MPa to typically 1000 MPa making

the sintering process rapid and effective. Generally, the electric field can be applied in a number of ways: pure DC (also called resistive sintering), pulsed DC or Microwave. Activated sintering using a pulsed DC has also been often referred to as Spark Plasma Sintering (SPS) in the literature, since the high current density is thought to induce a plasma at the inter-particle neck region. However, the generic term, Pulsed Electric Current Sintering (PECS) is also commonly used in reference to any type of current waveform other than pure DC.

In a typical SPS process, the powder sample is loaded in a cylindrical die and closed on the two sides by electrically conductive punches. For ease of separation after sintering and also to avoid any reaction between the punch and the sample, graphite papers are used as spacers. Sintering is carried out in vacuum and both pressure and electric current through an external power source is applied to the punches. The electric field control can be achieved in two ways: in the *temperature controlled* mode, the current to the punch and sample is supplied according to a pre-set temperature programme. The temperature is measured at the die surface with a pyrometer and the feedback is used to adjust the current supply accordingly. In the *current controlled* mode, a constant current is supplied to the sample and the temperature is monitored. Very high heating rates can be achieved limited only by the maximum current available from the power source. However, the actual temperature in SPS can be quite different from the measured temperatures for many reasons: the pyrometer measures the temperature at a niche in the die which is neither exactly on the sample surface nor in the surface interior - certain reports put this difference at ~50-100 K [Bernard and Guizard, 2007]; measured temperatures are usually the average values and give no indication of the very local temperatures that can actually exist between the particles. The overall electrical resistance - including the internal resistance of the voltage source and resistance of the bulk of the apparatus - controls the current flow and consequently, the Joule heating generated in the sample. Hence, in an SPS experiment, the total resistance, R_{total} can be written as:

$$(R)_{total} = (R)_{internal} + (R)_{contact} + (R)_{sample} + (R)_{bulk} \quad (1)$$

It has been found that for a constant applied current, the maximum resistance (and thereby the maximum joule heating) occurs at the punch/graphite contact surface, $R_{contact}$ [Giovanni Maizza *et al*, 2007, Munir Z A et al, 2006]. Moreover, the resistance of the sample, R_{sample} is continuously changing (as a function of the instantaneous porosity) and hence, the observed value of current in circuit is a product of the complex interplay of various parameters. The pulse frequency of the DC supply in a typical SPS process is split into an ON/OFF ratio of 12/2. The ON pulse in turn is split into sub pulses of milli second duration. All these parameters can be controlled by the user to achieve the best sintering conditions. Usually, only the heating rate and pressure are varied with the rest of the controls kept according to the factory settings.

While the quantum of publications on/using SPS has been steadily increasing, the basic process is far from being well understood; the answer to the fundamental question of whether a plasma is generated at the inter-particle contact area is still elusive. Another

intriguing fact is the observation of very low sintering activation energies, enhanced sintering rates and low sintering temperatures when the sample is subjected to a simultaneous pressure and electric field as in SPS. While some authors attribute this observation to electro-migration (i.e., diffusion under an electric field gradient) as a, 'sintering enhancer', it must be noted that electro-migration can be expected to play a serious role in the sintering of highly ionic compounds. But the observation that the activation energy can be equally low in predominantly covalent compounds like WC (the ionicity according to the Pauling scale is only ~1%) suggests that the field effect may not be the sole cause for the observed rapid kinetics. Thermodynamic arguments suggest that the applied pressure drives sintering while the electric field retards grain growth thereby achieving full densification with limited grain growth. A number of alternate mechanisms, which treat the GB as a separate phase have also been put forth [Dillon S J *et al*, 2009, Di Yang *et al*, 2010, Gupta V K *et al*, 2007]. However, while the outcome has been certainly encouraging, a clear and validated picture of the sintering mechanism under activated sintering is still lacking.

3. Isothermal and non-isothermal sintering

Sintering, like coarsening and grain growth is also a thermally activated process and hence an Arrhenius type of dependence on temperature is observed. The kinetics of fusion of two particles during sintering is usually studied either by measuring the neck to particle size ratio (x/a) or by measuring the macroscopic shrinkage using a dilatometer with respect to time. A number of theories have been developed to explain both shrinkage and neck growth during sintering [Ashby M F, 1974, Swinkels F B and Ashby M F, 1981, Beere W, 1974, Coble R L, 1958]. Such theories derive explicit relations connecting the shrinkage strain, ε ($=\Delta l/l_0$) or neck growth (x/a) to the time of sintering, t under isothermal conditions. Measurements of neck growth in ultrafine particles are difficult and therefore, the macroscopic shrinkage strain is instead measured and a suitable theory is chosen to study the kinetics. In any case, the sintering kinetics (either solid or liquid phase assisted) can be described by a generic equation of the type:

$$\varepsilon^m = \left(\frac{\Delta l}{l_0}\right)^m = \frac{Kt}{T} \tag{2}$$

where 'm' is the sintering exponent, t is the isothermal holding time and T is the hold temperature. The higher the value of m, the lower is the magnitude of shrinkage. The constant, $K = K(T)$ is the temperature dependant sintering constant and accommodates the interface energetics and transport kinetics of the sintering process via the surface energy, γ and the diffusion coefficient, D. The form of K can be related to temperature by an Arrhenius type equation,

$$K = K_0 e^{-Q/RT} \tag{3}$$

where Q refers to the activation energy for densification and R is the gas constant. The kinetic parameters can be evaluated easily by a simple modification of the two equations. Firstly, equation (2) gives:

$$ln(\varepsilon) = \frac{1}{m} ln\left(\frac{K}{T}\right) + \frac{1}{m} ln(t) \quad (4)$$

Therefore a plot of ln (ε) against ln (t) at constant T is a straight line with slope $1/m$. The sintering exponent 'm' can vary depending on the mechanism (diffusion path) and geometry of the sintering bodies. **Table 1** shows the various values of m available in the literature, modelled for the sintering of a pair of spherical particles.

The activation energy for sintering, Q can be determined in many ways: Utilizing the exponential dependence of K on T, and the m value determined earlier, we can write,

$$ln(T\varepsilon^m) = ln(K_0 t) - \frac{Q}{RT} \quad (5)$$

Hence a plot of ln ($T\varepsilon^m$) against $1/T$ at constant values of time, t should yield a straight line from which Q can be determined if the sintering exponent, m is known. Another equivalent method for determination of the activation energy of sintering in isothermal experiments is the time for constant fraction technique which is based on the measurement of a constant linear shrinkage fraction at different hold temperatures. The activation energy can then be determined by:

$$ln(t) = ln\left(\int_0^f [k_0 f(\varepsilon)]^{-1} dy\right) + \frac{Q}{RT} \quad (6)$$

where $f(\varepsilon)$ is the shrinkage strain – time curve.

A more common method of determining the activation energy without *apriori* knowledge of the sintering exponent, m is the Dorn's method [Bacmann J J and Cizeron G, 1968]. Here, the densification strain rates are evaluated at a constant time at different sintering temperatures so that the slope of a plot of ln($d\varepsilon/dt$) against $1/T$ would yield values of Q. Usually the Dorn method is associated with an error of ~8 to 10%. Provided the initial temperature instability during the first few minutes of isothermal hold is eliminated and if the system does not exhibit shrinkage saturation (asymptotic behaviour) very early during the hold period, both kinetic methods should yield the same values of activation energy.

Equations (2)-(6), hold only during the initial stages of sintering. At later stages of sintering, the free energy reduction accompanying grain growth exceeds that of neck growth. When neck formation is succeeded by interconnected pore structures, the intermediate stage is said to have started. This stage is usually reached after the compact attains 80% or greater of the final density. Compared to the initial stage, fewer models are available for this stage owing to two primary reasons: complicated pore/particle geometry and concurrent grain growth. Densification strain equations for the intermediate stage are primarily based on pore/particle geometries and the inter-relation between them. The frequently referred intermediate stage model is the tetrakaidecahedron model of Coble [Coble R L, 1961a, Coble R L, 1961b]. The appropriate shrinkage kinetics is derived in terms of porosity (pore fraction) rather than linear shrinkage and expressed for different mechanisms as follows:

Lattice diffusion without grain growth

$$P - P_0 = \frac{N_A D_v \Omega \gamma}{k_B T G^3} t \quad (7)$$

Lattice diffusion with grain growth

$$P - P_0 = \frac{N_A D_v \Omega \gamma}{k_B T G^3} ln(t) \quad (8)$$

Grain boundary diffusion without grain growth

$$P - P_0 = \left(\frac{N_A D_b w \Omega \gamma}{k_B T G^4}\right)^{2/3} t^{2/3} \quad (9)$$

where the terms have the following meanings: P_0 – initial porosity at $t = 0$ in the intermediate stage, P – final porosity, D_v, D_b – volume, grain boundary diffusivities, γ– surface energy, w –grain boundary width, Ω – atomic volume, G – grain size and the other terms have the usual meanings.

Non isothermal (also called *constant rate of heating*, CRH) sintering can also be analysed by suitable models. In this work, we employed the method of Young and Cutler [Young W S and Cutler I B, 1970] to determine the activation energy from a plot of ln(dε/dt) against 1/T. The slope determined from the plot is mQ (effective activation energy) and if either the mechanism (m is ½ for LD and ⅓ for GB diffusion) or activation energy (Q) is known *apriori* (from isothermal experiments), the other unknown can be determined. We used a combination of both isothermal and non-isothermal sintering to complement each for the kinetic studies reported in this work.

Diffusion pathway	Value of m	Reference
LD	0.46	Johnson and Cutler, 1963a
	0.5	Coble R L, 1958
	0.4	Kingery W D and Berg M, 1955
GB	0.31	Johnson and Cutler, 1963b
	0.33	Coble, 1958

Table 1. Values of the initial stage sintering exponent developed for model geometries. (LD and GB refer to lattice diffusion (i.e., volume) and grain boundary respectively).

4. Experiments

Commercially purchased *n*-WC powders without any pre-treatment were used for sintering. The particle size measured by BET was 70 nm and the powder composition included 0.4% O, 5 ppm Cr, 27 ppm Fe, 4 ppm Mo, 3 ppm Ca, 2 ppm Ni, <5 ppm Si and < 2 ppm Sn. Approximately 2.5 – 3 g of the powder was filled into a 10 mm diameter graphite die for spark plasma sintering (SPS) in a Dr SINTER LAB instrument. This SPS instrument has a dilatometer with an accuracy of 0.01 mm for measuring the instantaneous linear shrinkage. Temperature measurements were carried out using a radiation thermometer (pyrometer) that was focused on a small niche in the carbon die. Graphite sheets were used as spacers to separate the powder sample from the punch and die. After initial temperature stabilization at 873 K for 3 minutes, sintering was carried out in vacuum (< 4 Pa) at a constant heating rate of 50 K/min and a compressive stress of 40 MPa to various temperatures from 1073K to

1873 K. The samples were held at these temperatures for a period of 30 minutes while their shrinkage was continuously monitored using a dilatometer. For the non-isothermal sintering studies, two heating rates – 20 K/min and 50 K/min – were employed and the sintering process was assumed to be complete when the dilatometer showed no further change in shrinkage during two successive temperature measurements. All the samples were allowed to cool down to room temperature inside the chamber. Before analysis, the samples were first polished with fine diamond paste (1μm) and subsequently cleaned with ethanol in an ultrasonic bath. The densities of the samples were determined by the Archimedes method. All densities are reported relative to the density of pure WC (15.8 g/cc). Fractured and etched samples were used for the microstructure analysis. Before etching, the samples were cross sectioned, polished and cleaned as earlier. Conventional Murakami solution (H_2O+KOH+$K_3[Fe(CN)_6]$ in a volumetric ratio of 10:1:1) was used for etching the compacts. For TEM analysis, the cross sectioned samples were mechanically thinned to 100 μm, dimpled to a depth of 20 μm and then milled with Ar ions to electron transparency. Microstructure and phase analyses were carried out using XRD, FE SEM, EBSD and TEM. Grain size evaluation was performed using the FE SEM images (15000 X magnification) of the etched samples with the aid of an image analysis software (Image Pro-Plus). Approximately 150-200 grains from three different locations of a sample were randomly selected for the measurements. The boundaries were delineated either manually or auto segmented and the average diameter (average value of the diameters measured at 2° intervals and passing through the centroid of the selected grain) of the grains was calculated.

5. Results

5.1. Analysis of the sintering kinetics

Fig.1 shows the combined isothermal and non-isothermal shrinkage curves. The immediate point worthy of interest is that the CRH strain rate curve does not exhibit a unimodal, gaussian type behaviour that is generally observed in the non-isothermal sintering of many ceramics [Wang J and Raj R, 1990, Panda *et al*, 1989, Raj R and Bordia R K, 1984]. Instead, there are two peaks (at around 1450 K and 1900 K) leading to a broad plateau covering a rather large temperature interval (from approximately 1400 K to 1900 K). At the peak points in the CRH curve, the corresponding isothermal curves also show a large increase in strain which varies proportionally with the relative magnitude of the CRH sintering strain rate; in most of the low temperature regime, the isothermal sintering strains show saturation, implying that the sintering strains are critically dependant on the heating rate and the temperature of isothermal hold. In conventional sintering, the heating rate is usually assumed to be irrelevant to the kinetics as the sample is presumed to reach the isothermal sintering temperature very swiftly. Our comparison shows the explicit dependence of the isothermal curves on the non-isothermal sintering trajectory and sintering temperature. These preliminary results confirm that the sintering behaviour is not governed by a simple, single mechanism. In the same **Fig.1**, the stages are marked as Initial, Intermediate I and II for ease of analysis. Although the curve does not resemble the typical three stage sintering process, it does indeed show at first glance, the occurrence of sub-stages.

As mentioned in the previous sections, the relevant equations of sintering have to be applied only to the corresponding sintering stages. Delineating a particular sintering stage (initial, intermediate or final) can be carried out by real time observation of the microstructure. However, such a process is tedious and quite ambiguous, particularly if the particle size is of the order of a few tens or hundreds of nm. As a general rule, when the measured linear shrinkage strains are less than 5%, the dynamics can be assumed to be in the initial stage. With this presumption, the subsequent analysis was carried out for the temperature range 1073-1273 K. Linear shrinkage strains and calculated sintering exponent in the initial stage are shown in **Fig. 2a,b**. Clearly, while the net shrinkage strains are less than 5%, the *m* values are not consistent. Careful observation of the sintering strain curves revealed that at those temperatures where the *m* values were unreasonably large, the curves reached saturation and flattened at longer hold times. At those temperatures where the shrinkage did not saturate, the sintering exponents were estimated to be m_{1173}=1.46 and m_{1273}=2.14 (LD through defects and GB recreation respectively, in accordance with the models of Kingery et al, 1975 and Coble RL, 1958). This temperature range seems to be a transition regime between defect-assisted LD and the initiation of GB diffusion at higher temperatures. Irrespective of the sintering mechanism, the initial temperature range shows two characteristics: presence of a non densifying mechanism and end point densities.

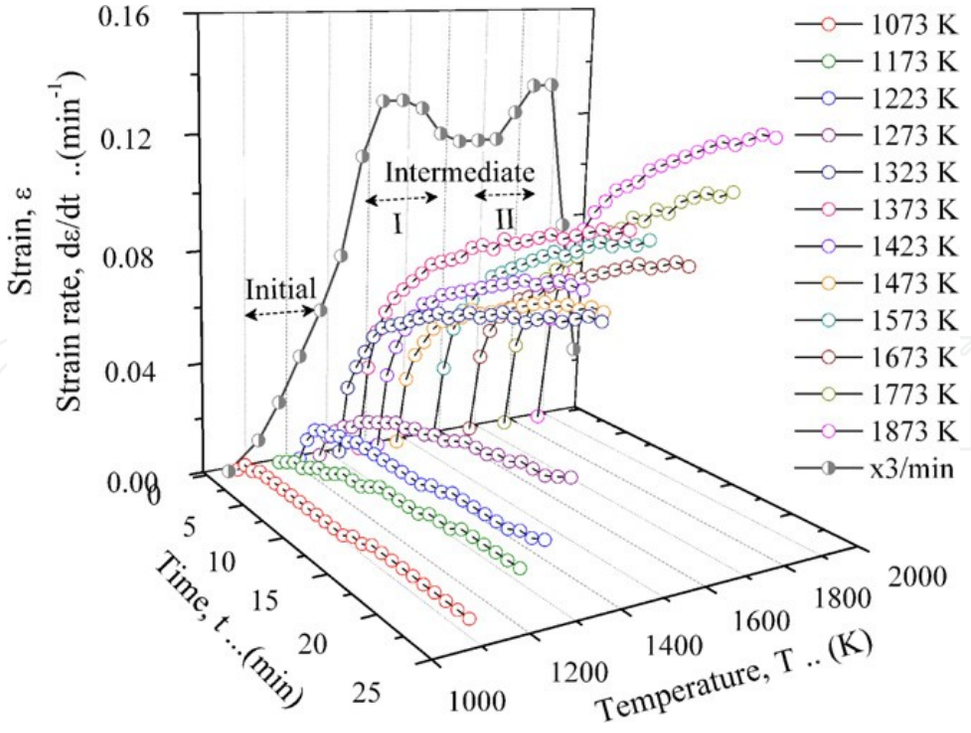


Figure 1. Isothermal and CRH sintering curves at different temperatures.

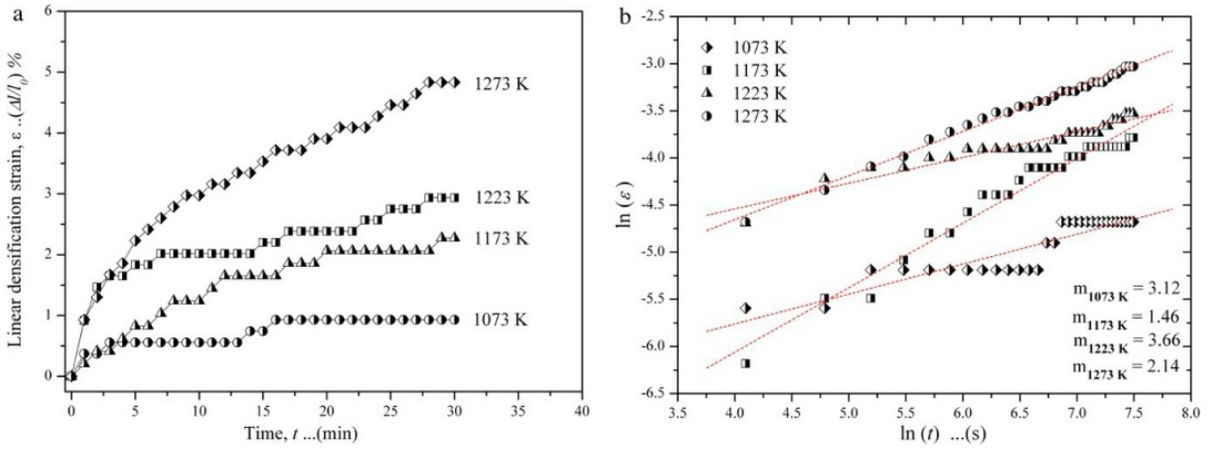


Figure 2. (a) Linear densification strains from 1073 K – 1273 K and (b) the corresponding sintering exponents calculated according to eqn. (4).

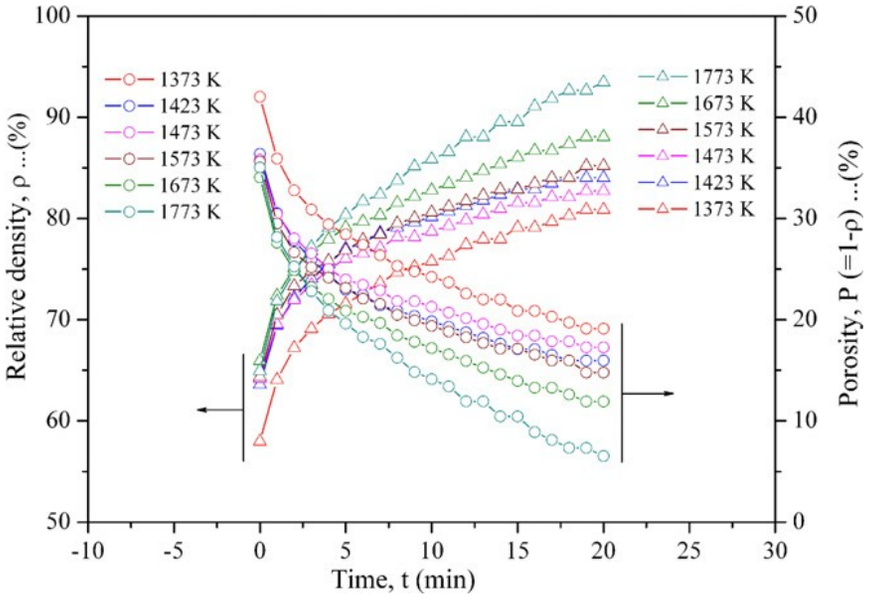


Figure 3. Porosity and relative densities at different intermediate temperatures.

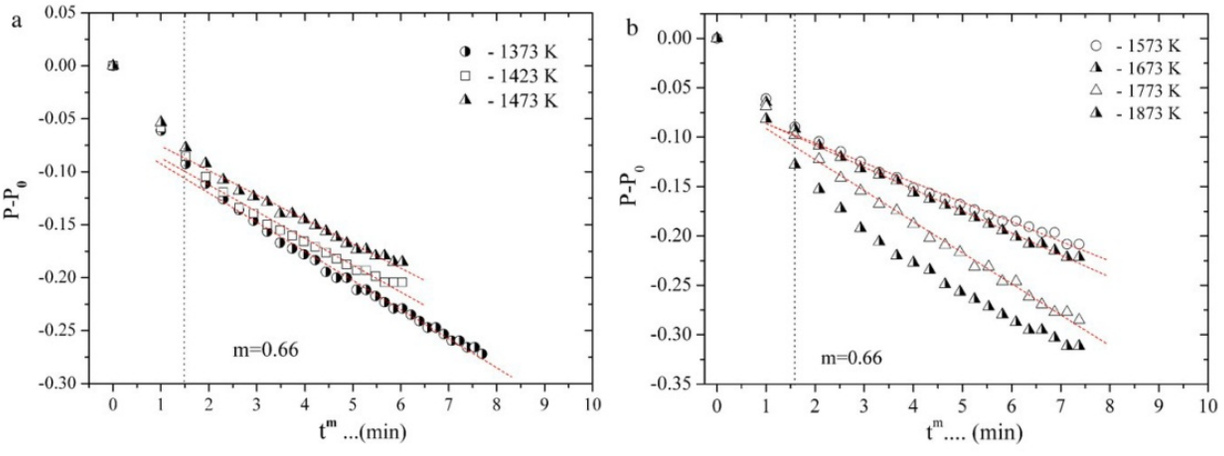


Figure 4. Plots of $P\text{-}P_0$ vs. t^m according to eqns. (7)-(9) between (a) 1373 – 1473 K and (b) 1573-1873 K.

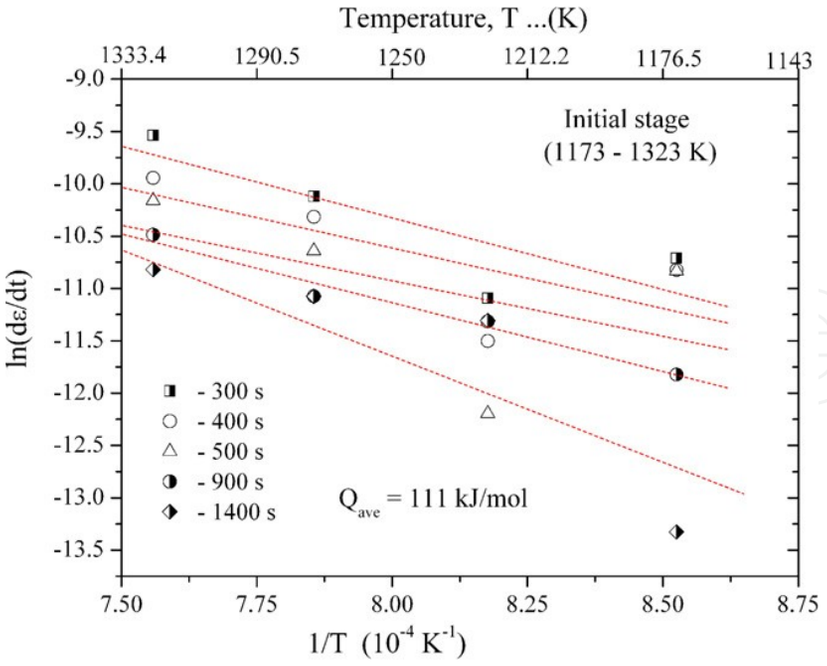


Figure 5. Calculation of apparent activation energy by Dorn's method.

For analysing the intermediate stage, the porosity fraction was estimated as $P = 1 - \rho$, where $\rho = (1 - \varepsilon)^3 \rho_f$ is the instantaneous density and ρ_f is the final density expressed as a fraction of the theoretical density. **Fig. 3** shows the porosity and relative densities of the samples at different temperatures in the intermediate stage. At the start of the isothermal hold period, the porosity was ≈35 to 42% (at various temperatures) which decreases to a value between 6 and 18% at the end of the hold period. It is interesting to note that although the density increases with the hold time, they are almost constant in a narrow range of temperature (1400 to 1573 K). The end density seems to be a strong function of the initial density at $t = 0$. **Fig. 4a,b** shows the subsequent kinetic analysis of the intermediate stage obtained by plotting $P\text{-}P_0$ against t^m. Most of the data points fall in a straight line when m=0.66, suggestive of Coble's grain boundary dominated sintering mechanism.

The apparent activation energy of sintering was calculated using the Dorn method. Only positive values of slope were considered. In the designated initial stage from 1173 K to 1323 K (**Fig. 5**), Q = 111 kJ/mol. In the final stages (1673– 1823 K), a small activation energy of 45 kJ/mol was calculated (figure not shown). The other temperature ranges could not be analyzed without ambiguity since sintering strains between the temperatures varied rapidly and our sampling interval (every 50 or 100 K) was inadequate to collect sufficient data points. The CRH experiments were hence considered for analysis at higher temperatures.

The sintering kinetics from the CRH experiments was also analysed. **Fig. 6** shows a plot of $\ln(Td\varepsilon/dT)$ vs. $1/T$ along with the measured values of the effective activation energy. Low heating rates were found to show transition stages clearly. Three different sintering stages can be identified from 1173 K to 1873 K by the change in slope: a first stage ranging from 1173 to 1273 K with mQ = 56.7 kJ/mol, a second stage from 1323 to 1473 K and mQ = 103.5 kJ/mol and a third stage with mQ = 41.35 kJ/mol between 1673 and 1823 K. Consistent with

the results of the Dorn method shown earlier, there was a narrow range with negative slope in the CRH experiments also between the second and third regions. The activation energy for sintering controlled by lattice diffusion (m = 1/2) in the I stage is Q I = 113.4 kJ/mol which agrees very well with the calculations of the Dorn method for isothermal sintering (Q = 111 kJ/mol). In the second stage, assuming GB diffusion (m = 1/3), Q I = 310.5 kJ/mol which closely corresponds to the activation energy for GB diffusion of C in WC [Bushmer C P and Crayton P H, 1971]. It should be mentioned however, that the appearance of this, 'second stage' depends on the heating rate (and consequently, the activation energy of the second stage is also a function of the heating rate). At low heating rates, a clear division between the first and second stages can be discerned by a change in slope, but at higher heating rates, it is impossible to differentiate between the first and second stage. The third stage clearly shows a very low activation energy, which could not be correlated to any reported solid state diffusion mechanism.

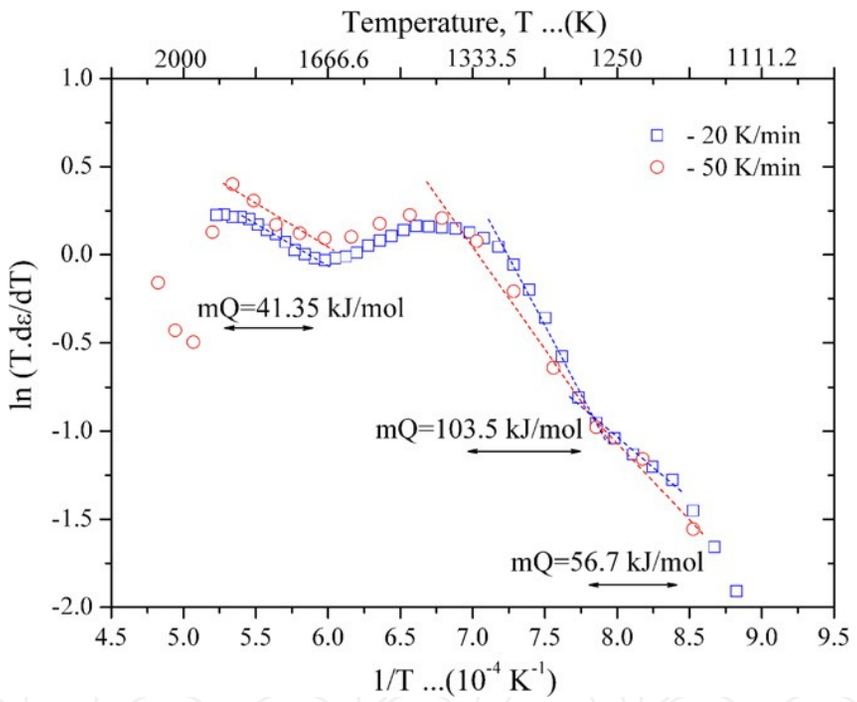


Figure 6. Calculation of effective activation energy from CRH experiments.

5.2. Microstructure analysis

A preliminary examination of the cross sections of the samples revealed that the edges of the completely densified compact was different from the bulk of the sample. **Fig. 7** shows the cross section SEM image and composition map of the sample by EPMA.

Clearly, huge abnormal grains populate the microstructure from the surface to a depth of nearly 30-40 μm. Interestingly, the chemical analysis of the surface by wavelength dispersive EPMA (Electron Probe Micro Analysis) also revealed a C deficient, W_2C layer on the surface. (It should be noted that the spatial resolution of the EPMA is rather low and therefore, while the W-rich layer on the surface is shown to be continuous, the region may actually comprise

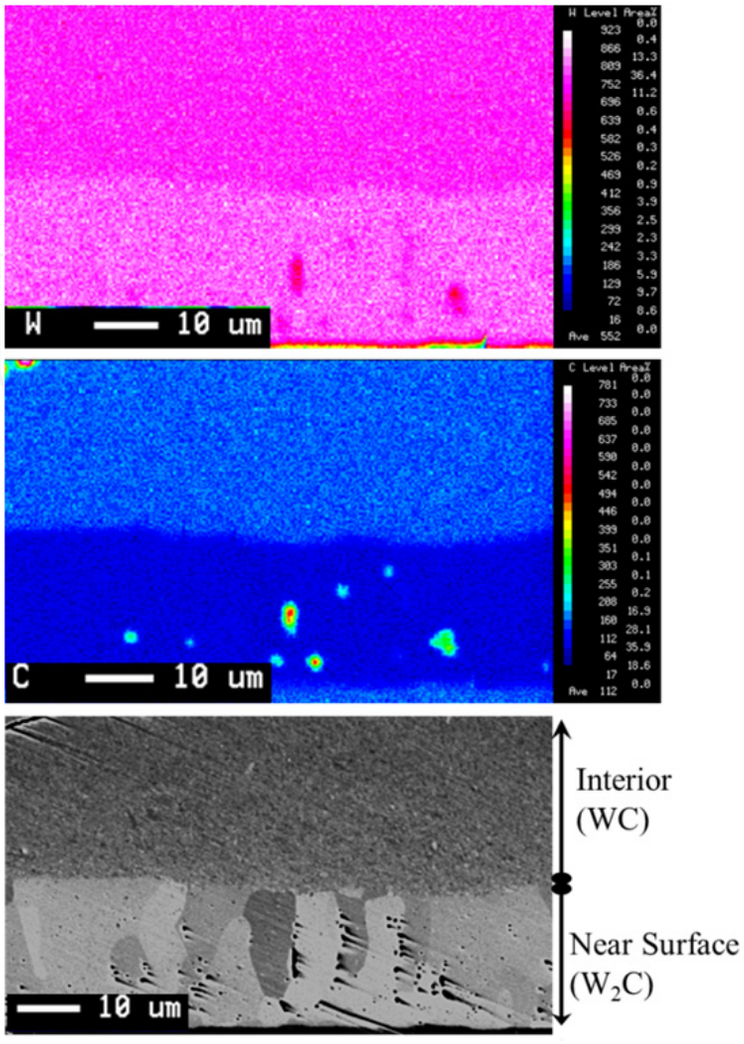


Figure 7. A cross-sectional composition map by EPMA near the graphite/WC interface of a completely sintered compact.

many small clusters of W_2C grains). Such differences in microstructure can occur by temperature gradients in the sample, resulting in a change in chemical composition at the punch/sample interface owing to the high activity of carbon in WC. Both hardness and fracture toughness measured on the surface and the interior showed that the surface was softer than the latter. With increasing heating rate, the grain size decreased with a corresponding increase in hardness, in accordance with the Hall-Petch effect, as reported elsewhere [Kumar A K N *et al*, 2010]. At higher loads, the hardness saturated to ≈2700 HV for the sample with the smallest grain size (with a sintering rate of 150 K/min, the final measured grain size was <300 nm), as shown in **Fig. 8**. The microstructure was also not uniform on the surface. The two phase regions existed as patches and were clearly discernible in the optical microscope. Indentation in these areas led to brittle fracture at the corners of the indent **(Fig. 9)**. Such a drastic change in the mechanical properties confirms the existence of W_2C, which is an embrittling phase in the W-C system [Luca Girardini *et al*, 2008]. More quantitative measurements of grain size and distribution were made using EBSD. The unique grain map (**Fig. 10a,b**) and quantitative grain size histogram plots

measured from the area fraction of the grains (**Fig. 11**) showed a bimodal grain size distribution in the surface with the peaks at ≈700 nm and 1500 nm, while in the interior, the grain size distribution was also bimodal but with the two peaks at ≈250 nm and 480 nm. The bimodal size distribution arises because of abnormal grain growth (AGG) – a characteristic trait of the carbides that exhibit facetted grain boundaries [Li *et al*, 2007, Byung-Kwon Yoon *et al*, 2005]. It is also interesting to note that the average grain size of both the normal and abnormal grains is higher on the surface than in the interior.

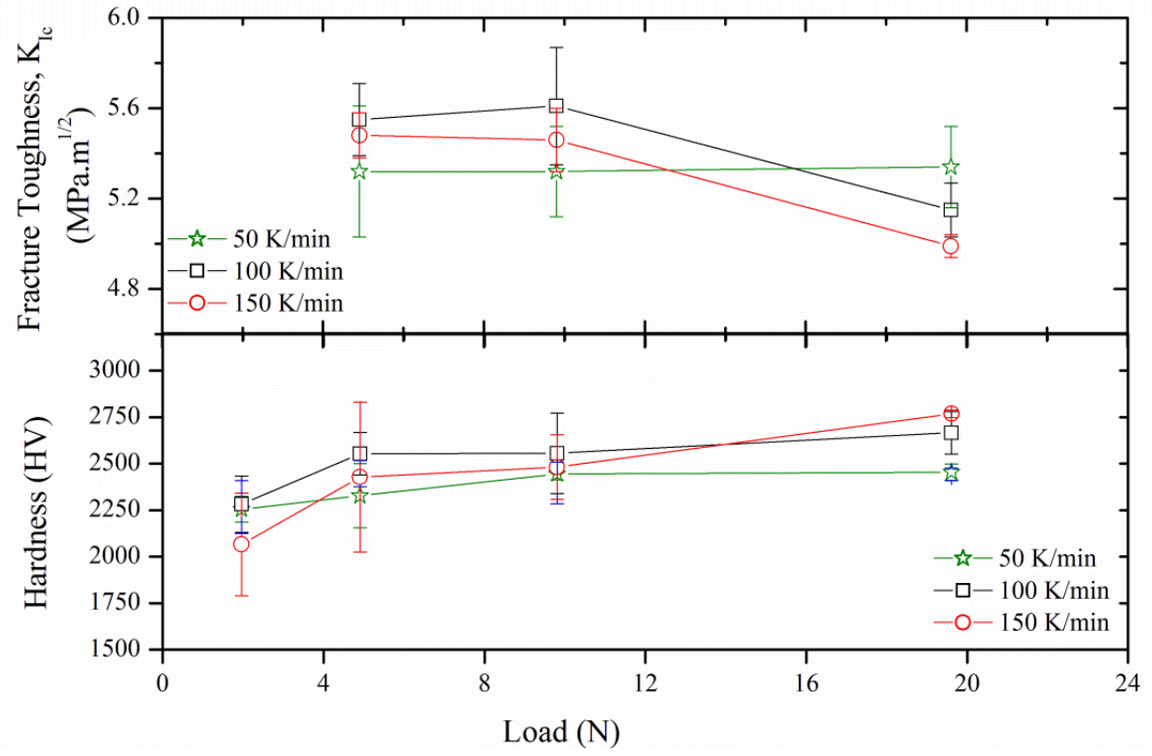


Figure 8. Hardness and fracture toughness of sintered *n*-WC compacts at different loads.

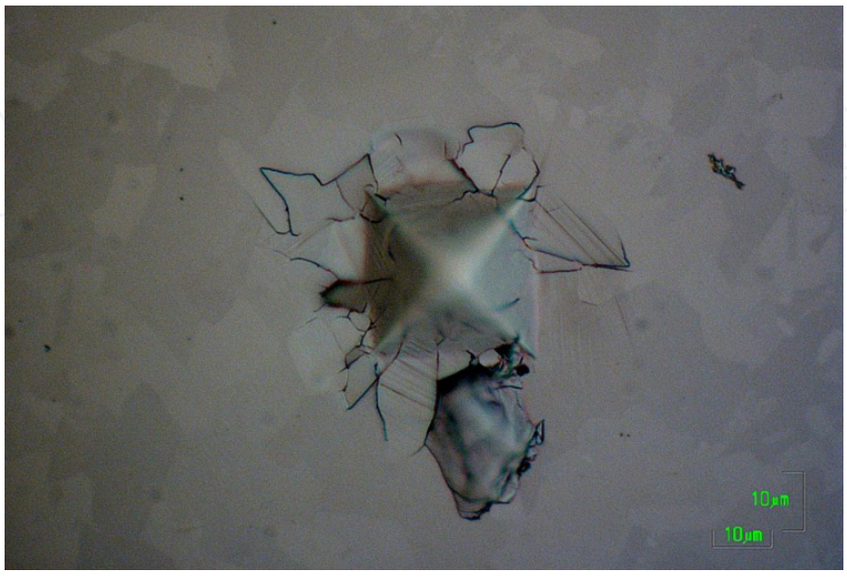


Figure 9. Brittle two-phase regions on the surface leading to indentation cracking.

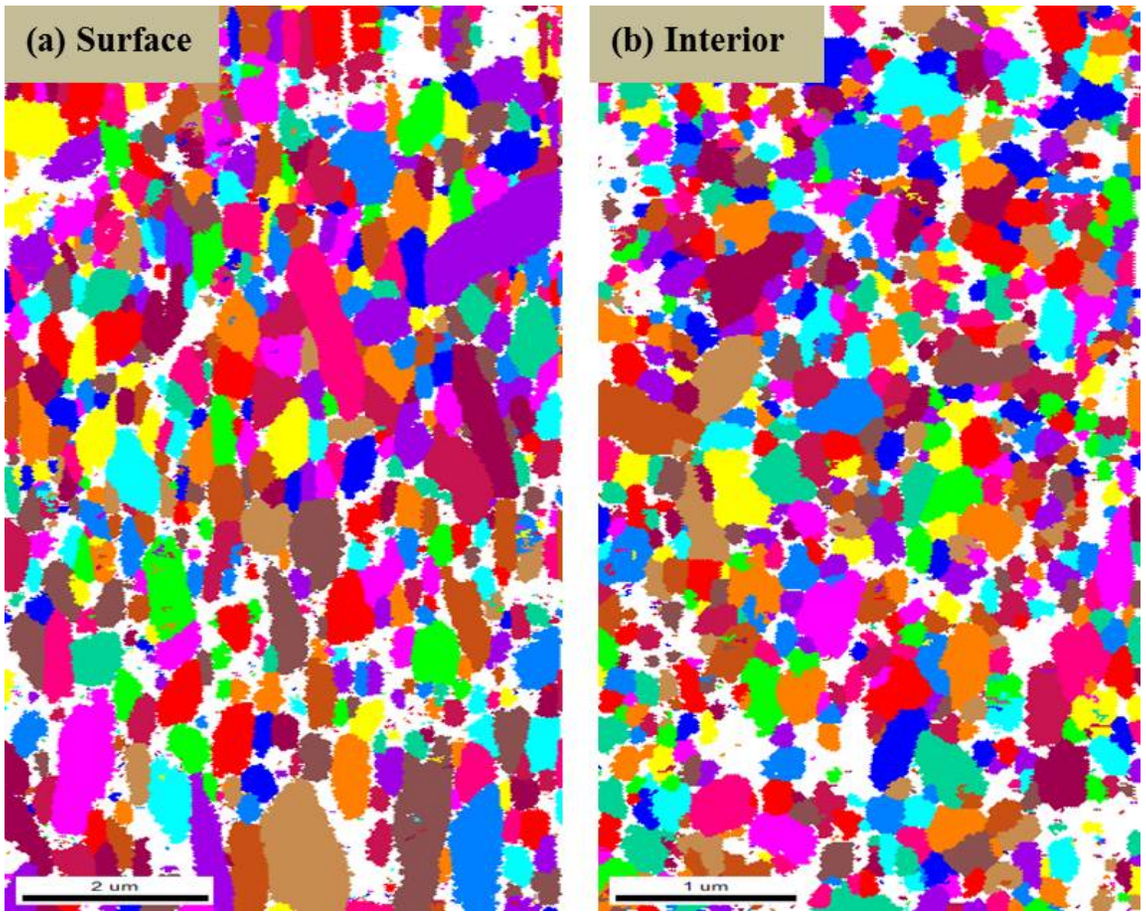


Figure 10. Unique colour grain map of the surface and interior of the samples by EBSD clearly showing larger grain size on the surface of the specimens.

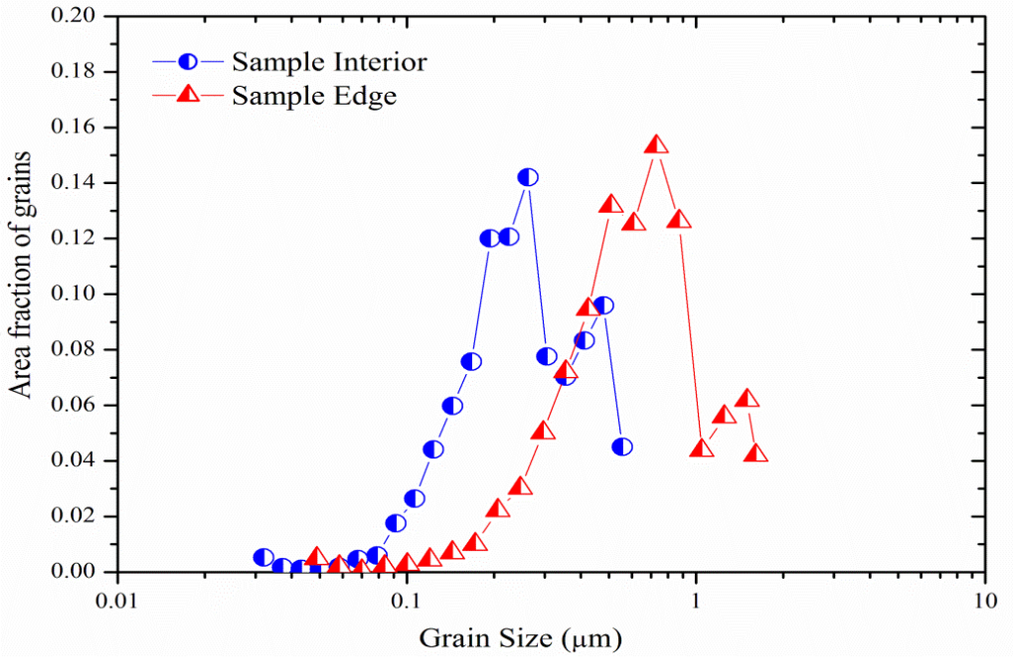


Figure 11. Grain size distributions by EBSD showing a bimodal distribution both on the surface and interior of the samples.

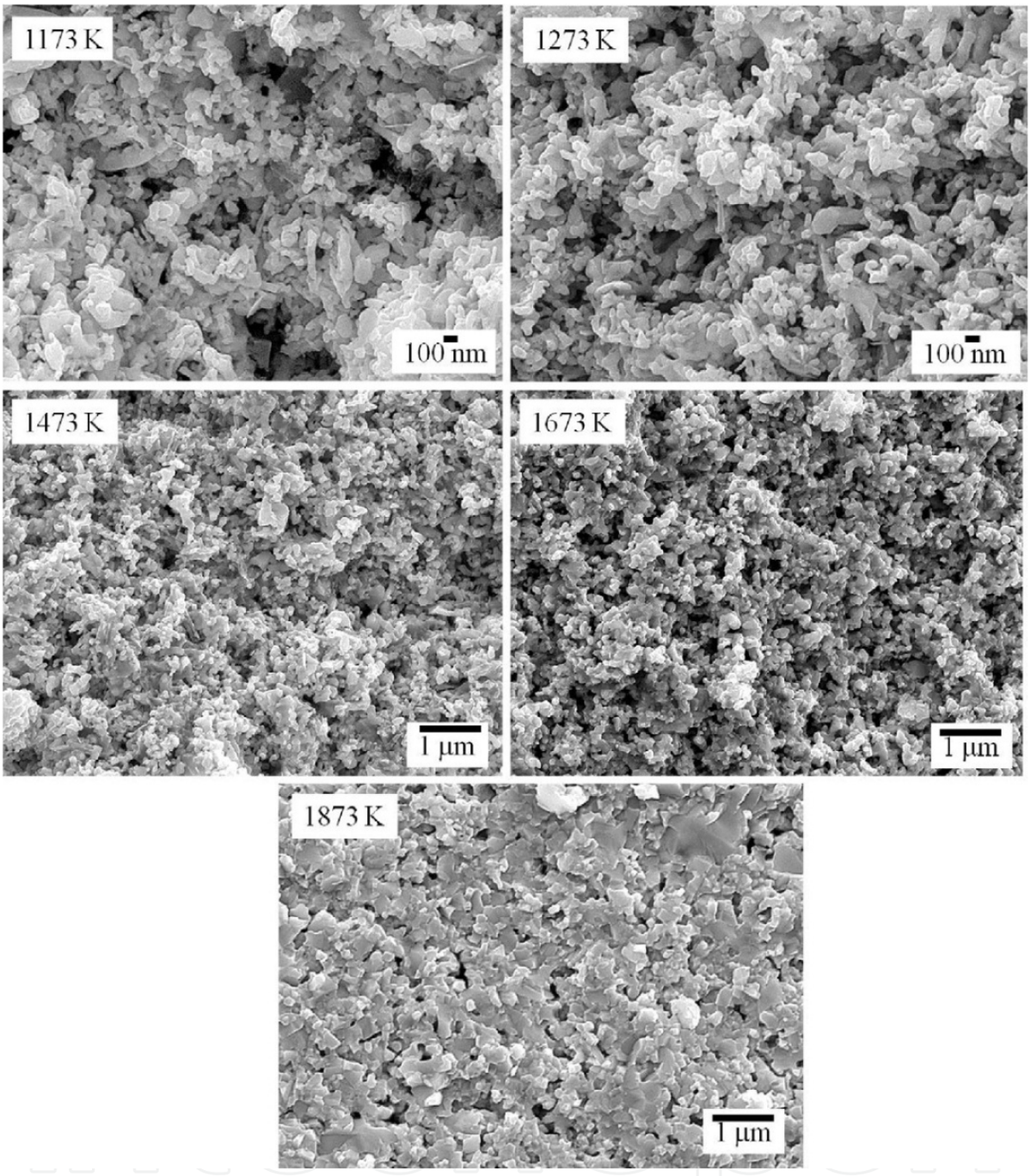


Figure 12. Microstructures of the compacts interrupted at various temperatures during sintering.

Fractured surfaces of the sintered compacts at various temperatures, observed by SEM are shown in **Fig. 12**. From 1173 K to 1323 K, the individual particles and bonded particles with necking can be discerned as a dispersed phase indicating the initial sintering stage. A few agglomerates can also be seen. From around 1373 K to 1773 K, large continuous pores were evident and this temperature range was considered to represent the intermediate stage of sintering. At 1873 K, most of the pore phase is pinched off, leading to the final sintering stage. However, the actual transition from the initial to intermediate stage sintering is rather vague as there are strong density gradients in the microstructure due to agglomeration. But

as a preliminary estimate, micrographs from these temperature ranges combined with the CRH-Iso sinter curves mentioned earlier can be assumed to represent the different sintering stages. While the SEM analysis does reveal the formation of agglomerates – thereby partly explaining the humps and dip in the CRH curve - the observation still does not account for the low activation energies measured by the kinetic analysis.

To probe the structure of the sintering particles further, the interrupted samples were also observed by TEM. A few samples were selected to understand the sintering behaviour: the original WC powder, samples sintered to 1323 K, 1473 K, 1673 K and the final densified compact. The WC powder was simply put on a grid and observed. **Fig. 13** shows a few micrographs of the powder sample viewed under the TEM. It was surely not a mono disperse powder. Agglomeration was clearly obvious and interestingly, a substantial fraction of particles containing stacking faults (SFs) were also seen. The extensive streaking of the spot patterns confirm that the steps observed on the particles are indeed SFs. The faults extended right across several grains diametrically to a length of nearly 2X the particle size, resembling shear bands. As no mechanical milling was conducted, it is likely that the SFs were introduced into the particles during the production stage itself. The clear proof of the occurrence of SFs in the initial particles is an important observation since lattice defects can impact the activation energy for diffusional sintering. Diffraction studies also revealed that the SFs were present only on the prismatic$\{10\bar{1}0\}$ planes and the basal {0001} planes were relatively free of defects.

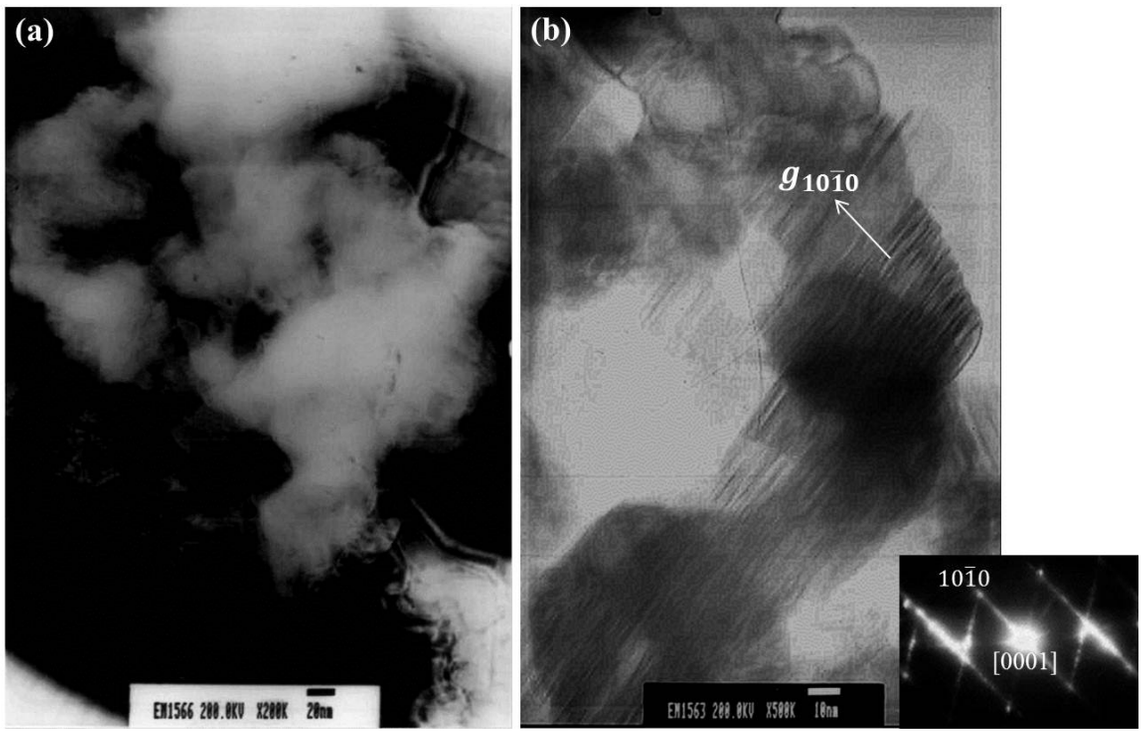


Figure 13. TEM micrographs of the *n*-WC powder showing agglomeration and stacking faults.

The sample sintered at 1323 K was observed next. It clearly showed signs of undergoing initial stage sintering (necking) in some of the separate particles that could be observed. The

necks between particles were almost 5 nm thick and interestingly, the neck and the entire surface of most of the particles showed a sort of spotty, recrystallized-like phase. This phase was marked by its characteristic dull appearance and hardly showed any diffraction contrast. While particle re-deposition during PIPS is most probably the reason for this observation of an amorphous surface layer, in a later section we also consider the effect of local temperature gradients leading to surface overheating of the powders that can be expected in SPS. There was a high density of thin SFs on the prism planes in these samples too (**Fig. 14a-c**).

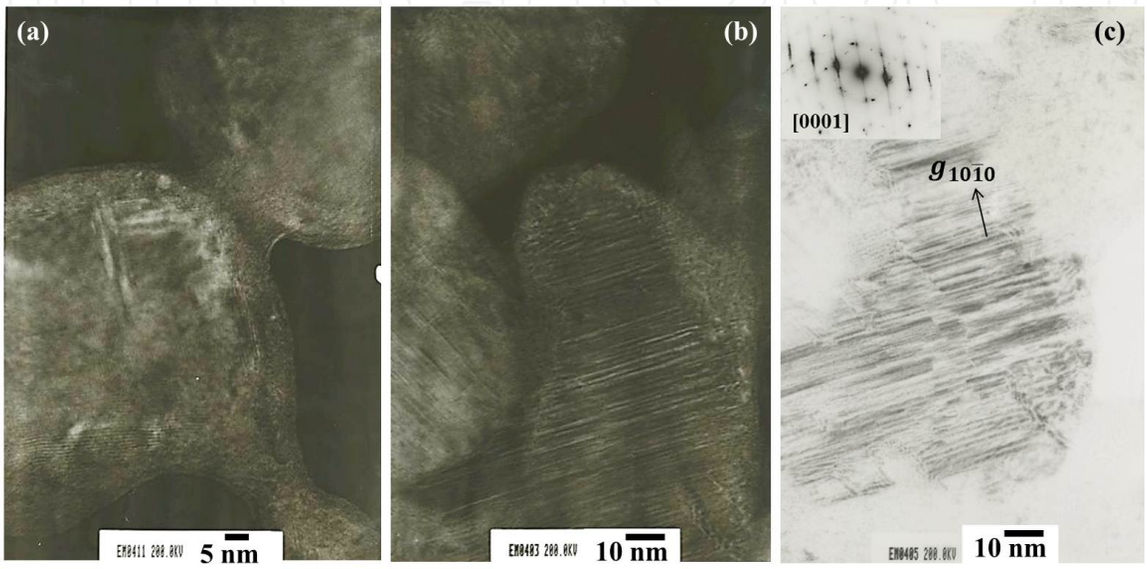


Figure 14. TEM micrographs of a sample sintered to 1323 K showing (a) necking (b) SFs with a thin amorphous GB phase and (c) Diffraction pattern (DP) and a dark field (DF) image confirming that the SFs populate the prismatic planes only.

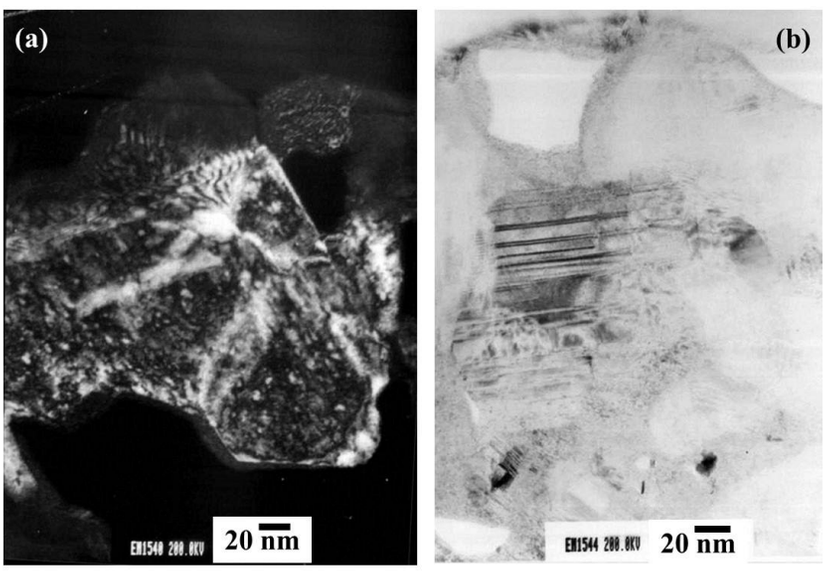


Figure 15. Sample sintered at 1473 K showing (a) a large grain with 3 or more sub grains and (b) SFs on prism planes.

The sample sintered at 1473 K showed evidence of necking, agglomeration and slight grain growth. In addition, a number of SFs could also be detected on similar prismatic planes – a continuation of the feature observed in the powders and the previous sample (**Fig. 15a-d**). The faults were well-formed and the fault line density in the observed grains was found to be lesser than that in the original powders.

The fourth sample that was investigated (1673 K) also showed the same features as that of the earlier sample sintered at 1473 K (**Fig. 16**). Necking was not observed, while the SFs were rather few and the grains were more facetted and clearly visible. In essence, the features were quite similar to the previous sample, except for a slight variation in the fraction of the phases and size of the grains. This sample also appeared to be in the intermediate stage of sintering.

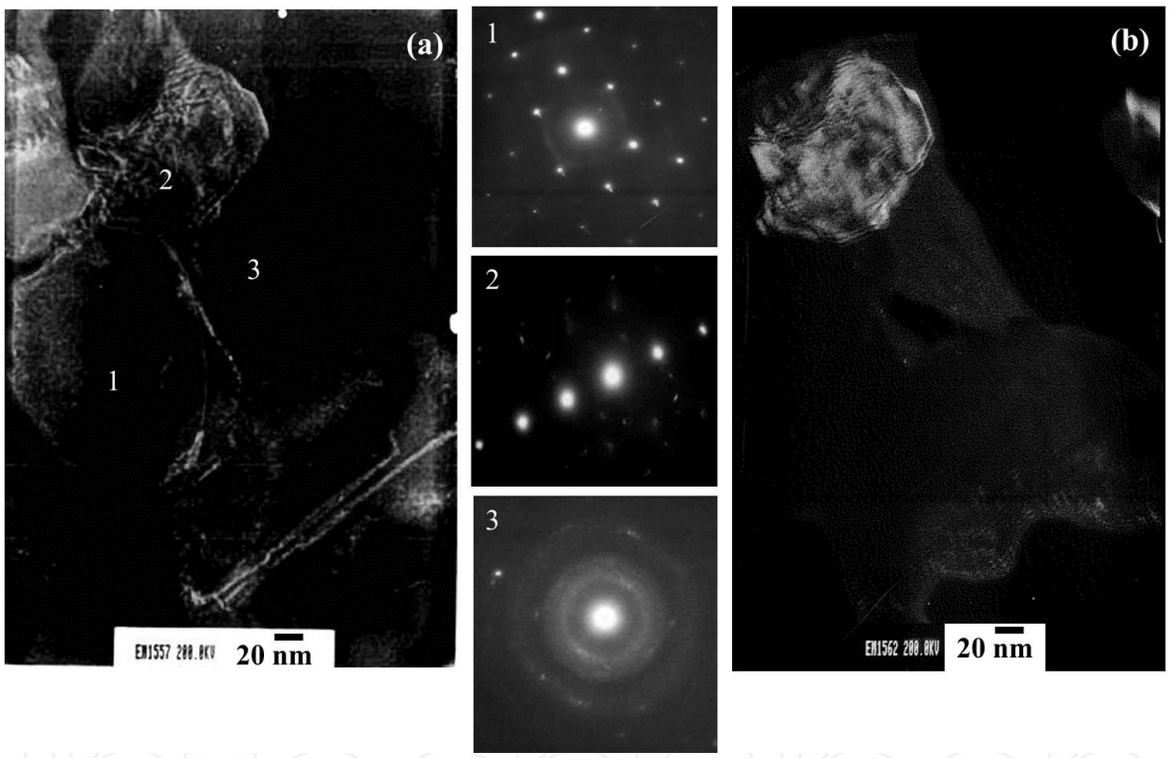


Figure 16. Sample sintered at 1673 K showing (a) three regions marked 1, 2 and 3 and their corresponding DPs. 1 is an almost defect-free grain imaged along [1$\bar{2}$10], 2 contains GB dislocations as seen from the multi beam condition in the corresponding DP and 3 is an amorphous pocket with a diffuse ring pattern (b) is the DF image from an excited spot in the DP in 2.

The final sintered sample (2073 K) showed well-formed grains (**Fig. 17**). While the specimen still contained some SFs in the small grains, in some of the larger grains instead of the SFs, twins were also observed (confirmed from the DPs which showed twin reflections). Interestingly, small grains of the semi-carbide W_2C measuring ≈50-100 nm could be seen in the sample (TEM samples were prepared from the cross section and not surface). All the grains were faceted and had sharp GBs. The grain growth into such well-formed structure seems to occur rather rapidly in the final stages of sintering with the annihilation of SFs, removal of the amorphous pockets and pore closure.

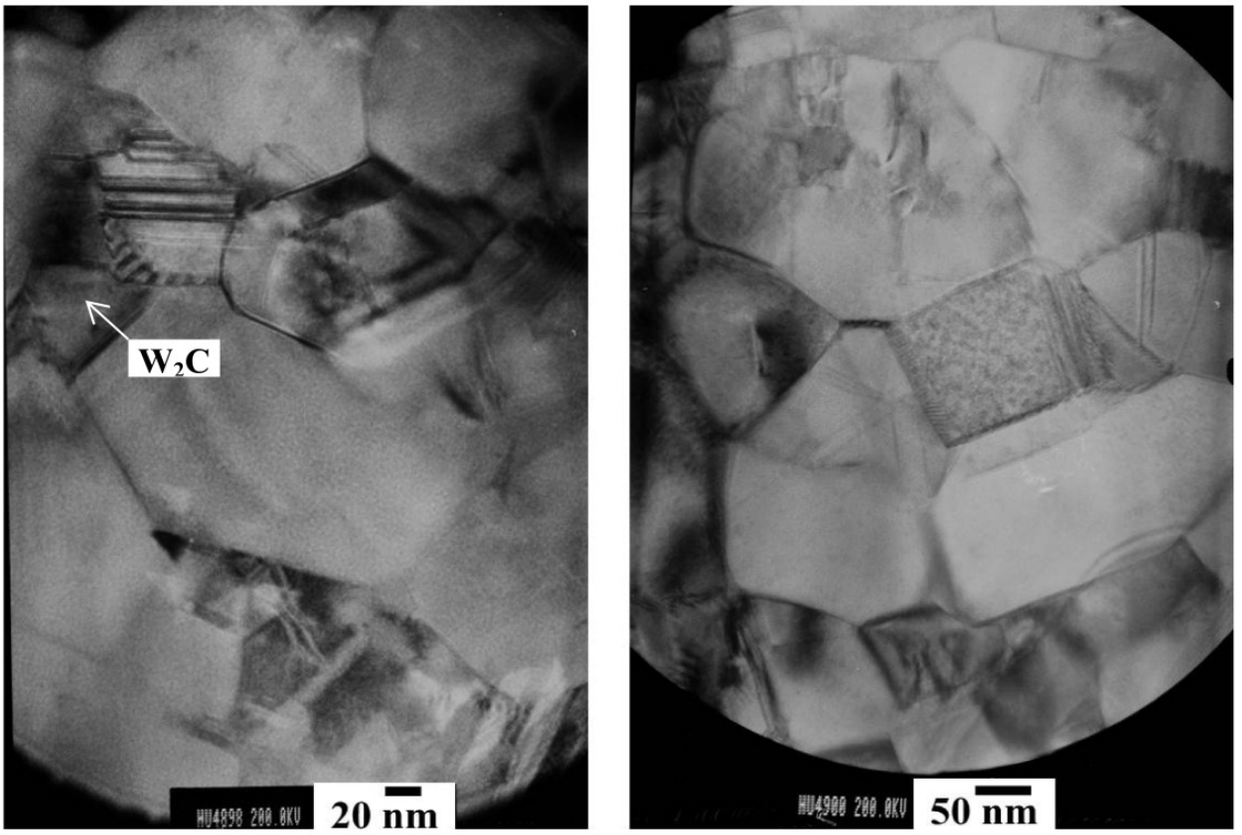


Figure 17. Sample sintered to almost full density at 2073 K showing a few SFs, but mostly well- formed faceted grains.

6. Discussion

The significant results of the kinetic and microstructural analyses detailed earlier are presented in an integrated way in **Fig. 18**. The measured relative densities and the corresponding grain size evolution together represent the sintering trajectory of the *n*-WC powder. It is seen that densification dominates during the initial stages up to ≈ 1350 K with the relative density increasing from ≈ 68% to 85%. Following this rapid densification, the density then *decreases* slightly; interestingly, grain growth is also insignificant during this stage. This is a surprising observation since while the densification rate ($d\varepsilon/dt$) can decrease owing to many factors (grain growth or the formation of a reaction product etc.), an actual decrease in the measured density cannot occur *unless the compact is subjected to a volumetric expansion or unless there is pore growth in the specimen*. A more clear picture arises when we convert the isothermal strains at different temperatures shown earlier in **Fig. 1** to instantaneous densities as shown in **Fig. 19**. We note immediately that near the vicinity of the first peak in the CRH experiment, while the isothermal densification strains are high, the *initial densities are also lower*. This simply means that the densification rate at any temperature is a function of the green density at that temperature. This behaviour persists over a small temperature range of ≈150 K after which at around 1500 K, the second stage of densification again begins; however, simultaneous grain growth is also observed here. This

multi-stage sintering process can be explained only by a combination of different densifying and non-densifying processes occurring simultaneously and sequentially at different stages. Since the sintering behaviour (*viz.*, the sintering kinetics and microstructure evolution) is influenced by the nano size of the particles, nature of the powder (agglomerates) and the activated sintering process – the effects of any of which on either the kinetics or microstructure are not exactly known, - we split the discussion into different segments in order not to mix up the issues and hence lend more clarity and focus to our overall analysis. The chief aims of this section are therefore to interpret the following observed phenomena: (i) the low sintering activation energies, (ii) occurrence of multiple sintering stages and (iii) the decrease in measured density at intermediate temperatures.

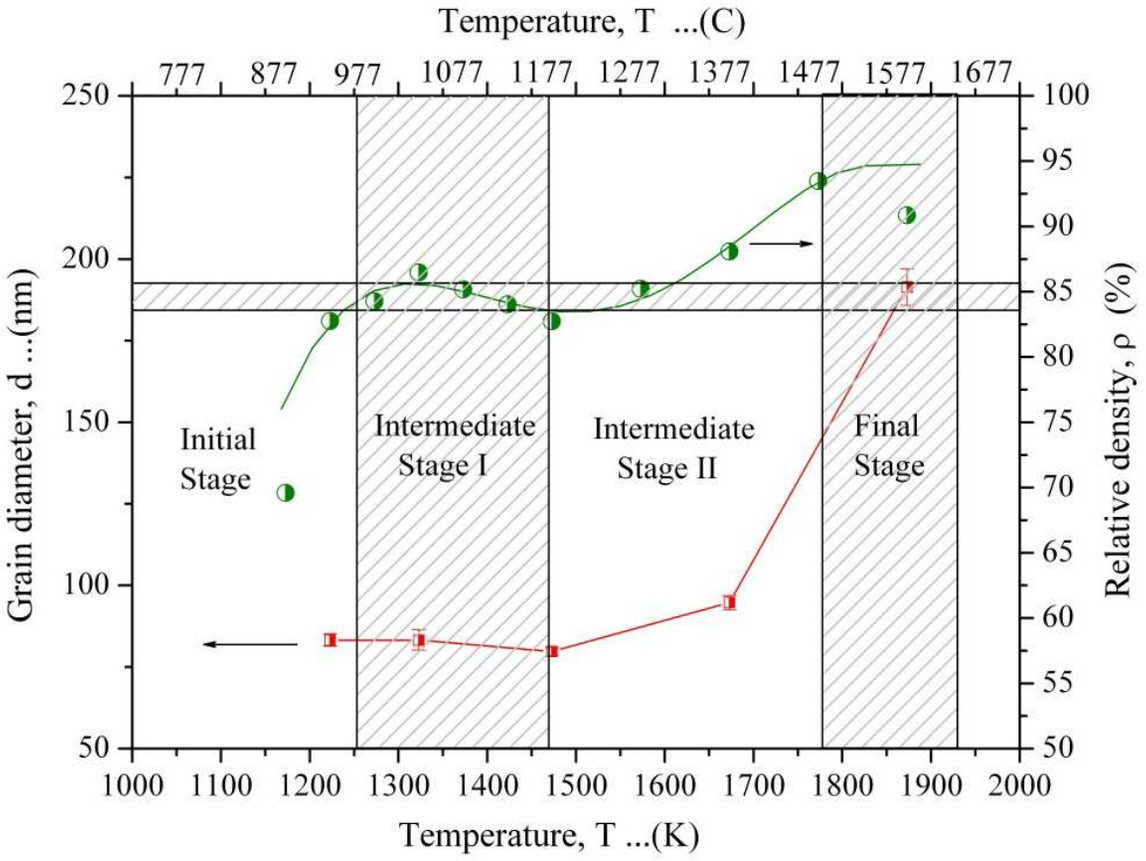


Figure 18. A sintering map showing variation of grain size and relative density with temperature.

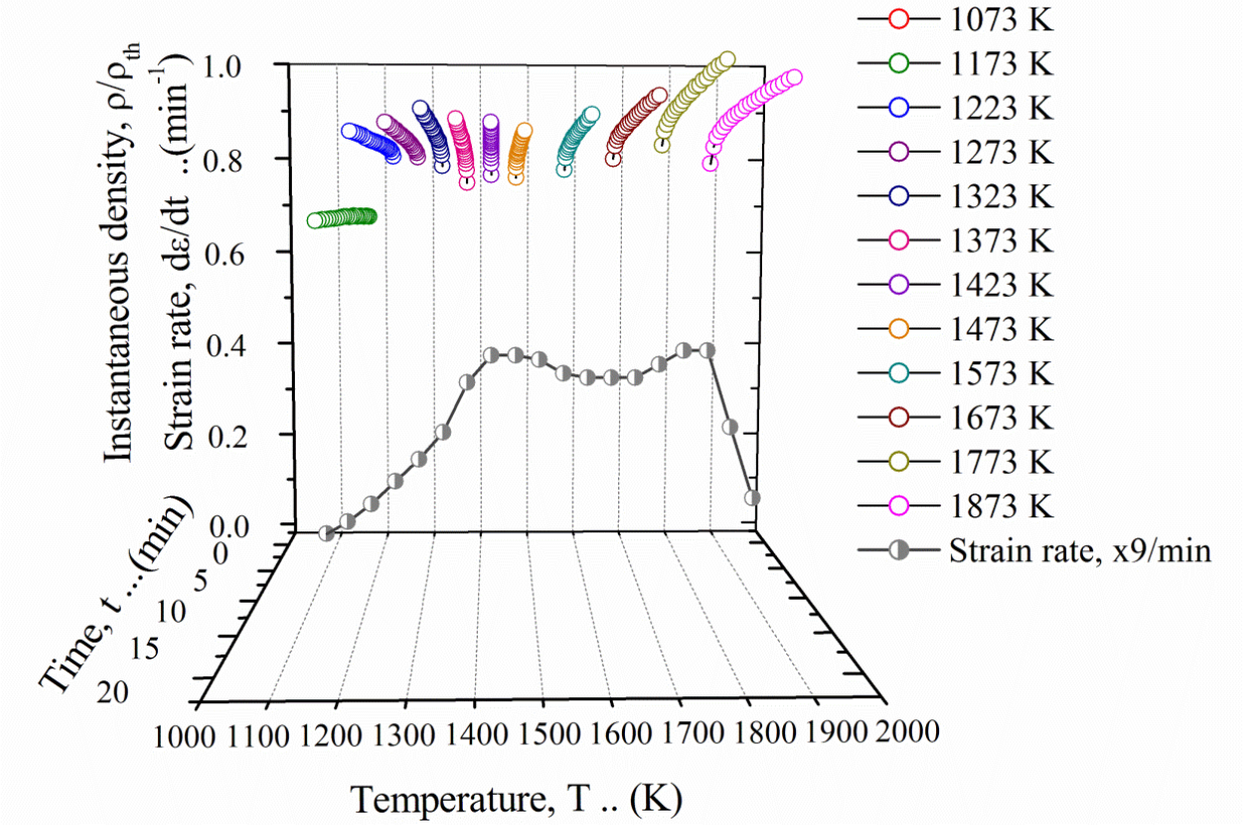


Figure 19. Comparison of CRH sintering rate and instantaneous densities during isothermal sintering (calculated by measuring the final density and using the relation, $\rho_i=(1-\varepsilon)^3\rho_f$)

6.1. Size effect on the sintering kinetics

Sintering of compounds (both ionic and covalent) occurs by the slowest species diffusing through the fastest route to establish the chemical equilibrium associated with the stoichiometry of the compound. In WC, carbon is generally considered to be more mobile than W. The crystal structure of WC is hcp (c/a=0.985) with C atoms occupying the interior positions in the unit cell. Yet, carbon cannot be equated to a regular interstitial atom in WC. This is because the tendency for formation of the W-C bond is quite strong. The origin of defects and the lower mechanical strength along the prism planes rather than on the basal planes can be traced back partly to this molecular origin [Nabarro F R N *et al*, 2008]. Yet, many direct and indirect evidences are available to support the fact that at higher temperatures, C is extremely active than W. For instance, the diffusion of tracer Carbon (^{14}C) in WC was found to occur initially by LD and later on by GB diffusion through the WC grains [Bushmer and Crayton, 1971]. Estimated values of D_v was very low compared to GB diffusion with the diffusivity ratio, D_{gb}/D_v being of the order of 10^3 (D_{gb} ~ 10^{-9} m^2 /s at 2238 K). The activation energy for GB diffusion of ^{14}C was estimated to be ≈ 300 kJ/mol. Another estimate provides a value of 10^{-22} m^2/s for lattice diffusion of ^{14}C in WC [Andrievky R A and Spivak I I, 1983]. Activation energies for the diffusion of W can be assumed to be higher. It should be noted that these estimates can be different when a liquid binder like Co is present since the WC molecule has to first dissociate into W and C, dissolve in the liquid and then

migrate to the re-deposition surface. Therefore in solid state sintering without Co, it might be expected that the diffusivity of the relatively immobile W should control the effective diffusivity during the sintering of WC. Yet surprisingly, our analysis suggests that the densification processes are activated by energies as low as 100 kJ/mol. There is a substantial body of evidence that suggests similar values of low activation energies that are comparable to our present results during the initial stage sintering of either WC nano particles or by activated sintering of large WC particles (discussed in the following section). Mugenstein and co-workers [Goren-Mugenstein G R *et al*, 1998] studied the initial stage sintering of WC powders with an average particle size 100-500 nm by conventional furnace sintering and employing the Dorn method, determined the activation energy to be 76 kJ/mol. Our calculations described in the earlier sections too showed values to be of the same order. Fang and co-workers [Fang Z *et al*, 2004] studied the sintering of various grades of WC-Co in a vacuum furnace. While they did not measure the kinetics, they did indeed observe that the onset temperature of sintering of the nano sized powders (50 nm particles) started 160 K below that of the micron sized powders. Moreover, since the nature of the sintering curves was similar for both particle sizes, they surmised that the densification steps were similar irrespective of particle size, but that the activation energy decreased with the size of the particles. Therefore, it seems that lowering of the activation energy can be achieved merely by reducing the particle size, atleast during the initial stage. Studies on certain other nano sized oxide ceramics also support the same view. Theunissen and co-workers [Theunissen G S A M. *et al*, 1993] studied conventional sintering of chemically synthesized ultrafine (8-50 nm) Y_2O_3-ZnO_2 ceramics and found that the activation energy was as low as 100 kJ/mol, which again did not correspond to any densifying diffusion mechanism. Comparison of these and many other results available in the literature [see for example, Dominguez O and Bigot J, 1995 (*n*-Fe), Kinemuchi Y and Watari K, 2008 (*n*-CeO_2), Victor Zamora *et al*, 2012 (*n*-ZrB_2), Li J G and Sun X, 2000 (*n*-Al_2O_3)] strongly support the view that a mere reduction in particle size can lower the activation energy for sintering. Fundamentally, this relates to a scaling down of a thermodynamic quantity with particle size, which can be analysed using Herring's scaling laws [Rahaman M N, (2003), Wenming Zeng *et al*, (1999)]. These laws basically compare the rate of sintering (densifying and non densifying) in different pathways for two dimensionally different particle systems. **Fig. 20** shows the sintering rates for two systems 1 and 2, as a function of the particle size ratio (R1/R2). The graph shows a cross-over when the particle size decreases (GB and Surface diffusion are significantly enhanced when R1<<R2). All the possible sintering mechanisms in a system can therefore be weighed on this scale simply as a function of particle size, provided all other factors are unchanged. Zeng and co-workers [Wenming Zeng *et al*, (1999)] used a similar type of semi-quantitative analysis and pointed out that, theoretically the sintering temperature (and hence activation energy) of pure α-Al_2O_3 can decrease from 1773 K for an initial powder size of 600 nm to 1498 K for LD and even lower to 1423 K for GB diffusion as the particle size decreases to 60 nm. In support of their argument, they even point out to some relevant experimental reports published elsewhere. The most probable explanation for all these various observations is that the surface and GBs of nano powders are easily activated and play a major role in lowering the sintering temperature and activation energy, irrespective

of whether other diffusion routes (LD, diffusion through defects etc.) dominate sintering in similar systems with a larger initial particle size. The same phenomenon can also be assumed to occur in *n*-WC powders. The presence of excessive planar defects also obfuscates the atomic diffusivity leading to rapid sintering. From the TEM micrographs, it is seen that the SFs dominate the microstructure until 1473 K, which act as short-circuit diffusion paths for sintering. However, while the particle size can be argued to lower the activation energy, it still does not explain the end point densities observed in most of the initial temperature range (shown in **Figs. 1, 19** earlier). Neither does the fact that surface diffusion is enhanced imply that shrinkage is also enhanced, since surface diffusion, unlike GB diffusion, is a non densifying sintering mechanism. Therefore, in addition to the particle size effect, there are other factors that control the sintering of the *n*-WC powders in the present case.

Direct observation of the presence of hard agglomerates (described in the following section) and the flattening of the shrinkage strain curves at low temperatures point to a mechanism of *particle rearrangement* (PR) that can induce a rapid initial densification but eventually leads to a saturation density. PR usually occurs at low temperatures, starts with a minor shrinkage and leads to an end point density when the closest packing is reached. This type of densification by rearrangement can be enhanced in the presence of surface diffusion, and GB sliding – both of which can be assumed to occur in the green compact. Most of the defects observed in the powders and low temperature compacts run diametrically across the particles and therefore can be equated to GB dislocations which can easily lead to GB sliding. The low sintering activation energy observed during the initial stage may therefore be attributed to a densification mechanism brought about by a combination of PR assisted by surface diffusion (SD) leading to GB sliding. This mechanism explains not only the low activation energy but also the saturation shrinkage strains observed in the low temperature region of the Iso-CRH curves.

6.2. Influence of agglomeration

Nano powders, owing to their high surface area to volume ratio, are characterized by a high surface energy. This leads to a difference in the chemical potential of the atomic species constituting the particle at the interior and surface and forms the chief driving force for agglomeration or aggregation. Such agglomerated nano powders are characterised by small groups of particles demarcated by GBs that in turn coalesce to form larger aggregates with pore boundaries [Lange F F, 1984]. This results in a totally non uniform microstructure leading to differential densification and multiple routes to sintering. Hence, the concept of the fastest diffusion route during sintering becomes complicated as intra agglomerate pores may densify easily while the larger pores may require higher energies for densification.

Fig. 21 shows a high magnification FE-SEM micrograph of a compact interrupted at 1073 K and also the initial powder, which shows a composite phase consisting of both individual particles and clusters of connected particles that have undergone necking. The clusters are hard agglomerates that persist even after the application of external pressure (40-50 MPa).

Unlike the soft agglomerates that form by weak van der Waals/electrostatic bonding and constitute inter agglomerate bridges, the hard agglomerates are formed by solid state diffusional bonding. In all the samples studied, the green density (before sintering) was less than 43%. It is clear that while the initial stage may be controlled by PR, the intermediate stage is governed by agglomerate evolution. When agglomerates form, internal density gradients are set up leading to a large pore size distribution. Consequently, sintering sub-stages are introduced in the intermediate stage by the differences in the sintering kinetics of the inter and intra agglomerate pores.

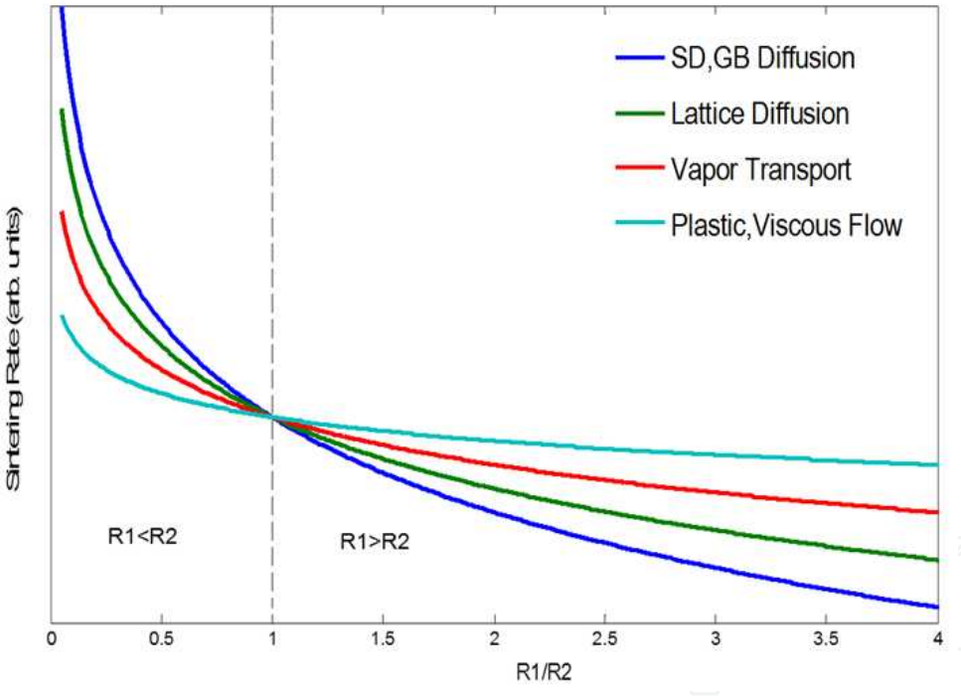


Figure 20. Dominance of various sintering mechanisms as a function of particle size calculated using Herring's scaling law.

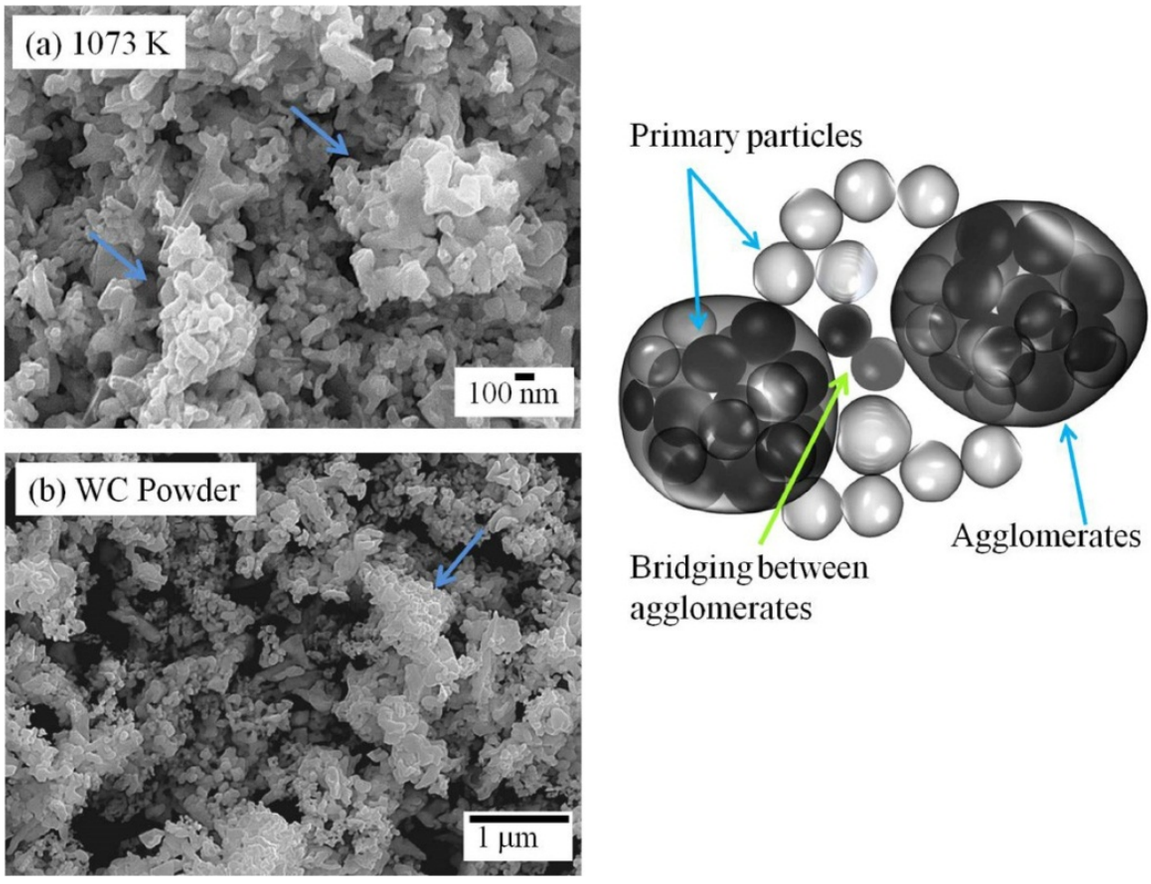


Figure 21. FE-SEM image of WC powder and compact sintered at 1073 K showing agglomeration. On the right is a schematic of the general low temperature microstructure.

Fig. 22(a–c) shows the high magnification microstructure of the samples from 1373 K to 1573 K. The agglomerates are enhanced and importantly, two different types of pore morphologies can be clearly distinguished: long, continuous inter-agglomerate pores and small disconnected intra-agglomerate pores (inter-particle pores). With increase in temperature, the individual agglomerates densify by sintering and slight grain growth, while there is not much observable change in the nature of the inter-agglomerate pores. At 1673 K, the grains can be clearly discerned and the intra-agglomerate pores have almost vanished, replaced by continuous pores (**Fig. 22d**). At still higher temperatures, (1873 K), the continuous pores become isolated and pinched-off resembling the final sintering stage (**Fig. 22e**). It is clear that the intermediate stage and much of the entire densification process is governed by agglomerate evolution.

Presence of hard agglomerates can partly explain the occurrence of sub-stages observed in the sintering rate curves. Initially, at low temperatures (T≤1423 K), there is a rapid increase in the densification rate of the compact. This occurs both by compaction of the agglomerates (contribution of intra-agglomerate sintering, which is expected to be low) and by rearrangement of agglomerates (inter-agglomerate sintering). The end densities increase to around 80%. This initial rapid shrinkage is followed by a saturation of the densification rate in the CRH curve. But interestingly, isothermal holds at these temperatures seem to induce high sintering strains. From this until ≈1623 K, the sintering rate decreases while the

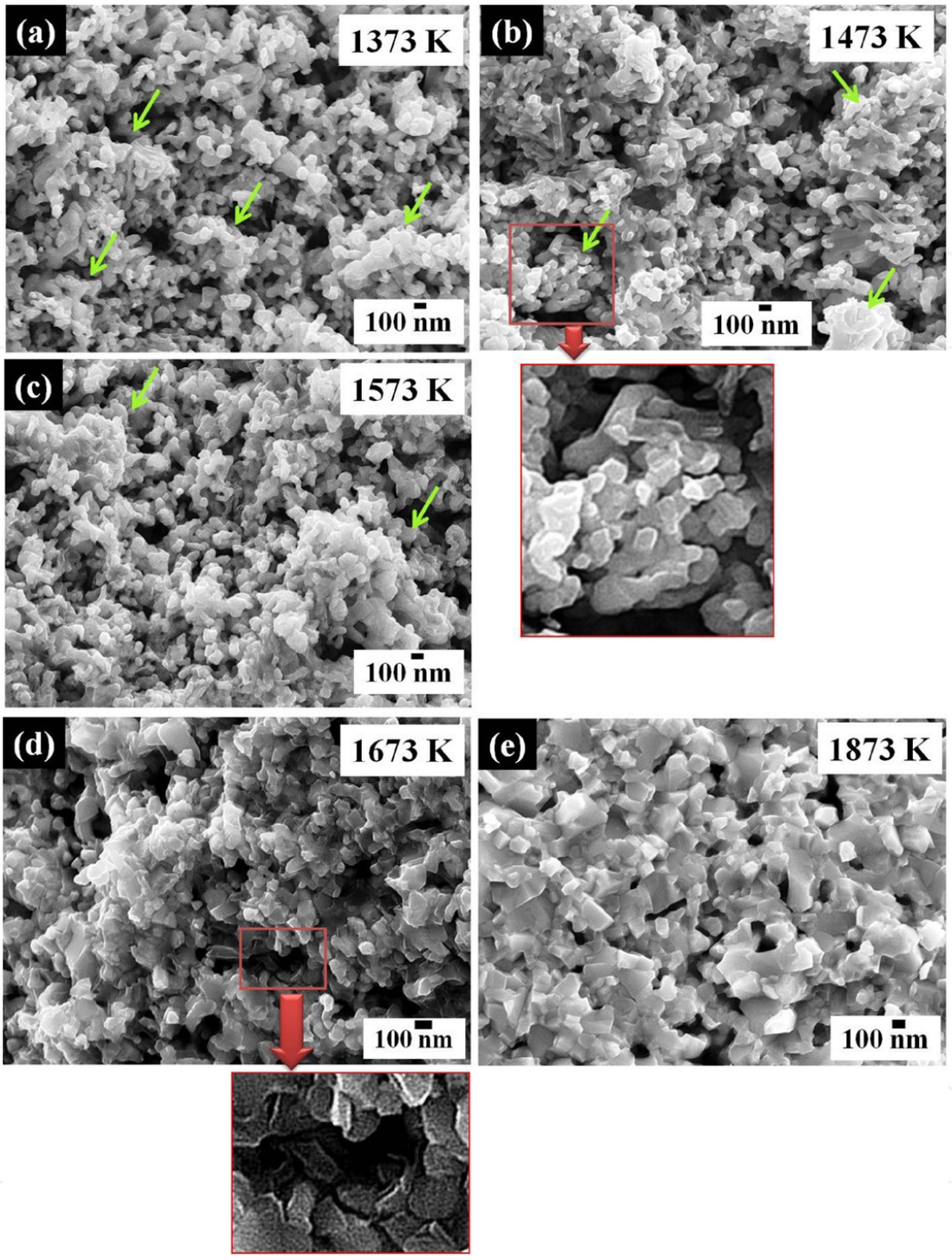


Figure 22. High magnification FE-SEM images of the intermediate sintering stage showing evolution of agglomerates.

isothermal sintering strains continuously increase. The decrease in the non-isothermal shrinkage rate can be explained on the basis of the energetics of the sintering of agglomerated powders: following the formation of stable agglomerates, the fraction of intra agglomerate pores is significantly reduced. From this point, the sinterability of inter agglomerate pores controls the densification rate. But this is also prevented because of the

large pore co-ordination number N_c. The dihedral angle (φ) in WC– Co is reported to vary between 30° and 120° [Gurland J, 1977]. WC (and in general, most of the transition metal carbides) exhibit facetted GBs and therefore the dihedral angle can vary drastically between different GBs. However, a statistical average of 75° can be assumed for φ. The approximate value for the critical pore co-ordination number, N_c can then be calculated from [Kingery et al, 1975]:

$$N_c = \frac{360}{180-\varphi} \tag{10}$$

where φ is the dihedral angle between the particles in the agglomerate. It turns out that N_c in this case is 3.6. Our microstructural observation show agglomerates that are co-ordinated by a far larger number of particles (**Fig. 22**) which clearly explains why the agglomerate sintering rate faces a thermodynamic barrier. This inter-agglomerate pore stability retards the shrinkage rate in the intermediate stage. Following the dip in shrinkage strain rate, there is a passive period over which the system tries to evolve by *particle growth within the agglomerates*. The massive grain growth leads to a breakup of the agglomerate identity into large grains and the stable inter agglomerate pores now start to sinter. As the agglomerates continuously convert into large grains, the pores start to shrink rapidly, surpassing the grain growth rate. Hence concurrent grain growth supports shrinkage until the continuous pores are eliminated and the isolated pore structure resembling the final stage appears. The relative densities increase to nearly 94% during this stage. The final stage of sintering is reached at temperatures above 1773 K when the pore phases are pinched off which again results in a reduction of the densification rate. Bimodal shrinkage rates seem to be a signature trait of agglomeration-induced densification and have been commonly reported in the literature [Lanfredi S *et al*, 2000, Jiang X X, 1994]. Non agglomerated powders show only one sintering rate maxima while agglomerated powders usually show double maxima for the bimodal pore size distributions [Nobre M A L *et al*, 1996, Shi J L *et al*, 1994, Duran P *et al*, 1996, Knorr P *et al*, 2000].

However, while the agglomerate evolution mechanism explains the sintering rate curve, it does not explain the instantaneous densification curves derived from the isothermal shrinkage data. As mentioned previously, the observation that the measured densities decrease with increase in temperature implies pore growth. Sometimes, coarsening can also lead to a decrease in density. But actual measurements do not show significant coarsening to occur in this temperature interval. Pore growth occurs to reduce the total free energy of the powder system:

$$\Delta G = \gamma_{gb}\Delta A_{gb} + \gamma_{s-v}\Delta A_{s-v} \tag{11}$$

where, γ refers to the energy of either a GB or pore and A_{gb}, $A_{s\text{-}v}$ are the corresponding areas. Under conditions, when $\gamma_{s\text{-}v} < \gamma_{gb}$, pore growth can occur. This can happen particularly when there is oxidation of the particles at high temperatures that reduces the surface energy of the particles. X-ray diffractograms of the samples at various temperatures are shown in **Fig 23**. At about 1300 K, it is observed that small peaks of WO_3 show up. In addition, from the earlier TEM micrographs, it is clear that there is a tendency for dissociation of WC leading to

oxidation of the particles. Therefore, it is probable that the oxidation of the WC particles could have led to the growth of pores. WO_3 has a high vapour pressure and therefore evaporates as it forms. It is probable that this continuous formation and evaporation of WO_3 leads to an increase in porosity (which lowers the density) while isothermal holding at these temperatures leads to an increase in densification due to the applied stress and continuous repacking of agglomerates. Liu *et al* [Dean-Mo Liu *et al*, 1999] reported a detailed study on the influence of agglomeration of zirconia (ZrO_2) powder. Their observation corresponds very well with our experiments: systems with a lower green density and which consequently are highly agglomerated show the maximum sintering rate and reach full density. The densification rate below the first maximum in the CRH curve corresponds to regions where isothermal sintering can be carried out. Similar results have been reported for *n*-MgO too by Itatani *et al*, [Itatani K *et al*, 1993] who show that a lower green density increases final densities of compacts. While these previous reports have not studied the isothermal and non-isothermal sintering behaviour at any particular temperature, they assume that coarsening could be the reason for the low densities at certain temperatures. This point is still ambiguous and requires further detailed investigations to clarify the actual mechanism. But as Kellet and Lange have pointed out earlier, for a fixed sintering temperature and time, the end point density is proportional to the bulk density of the powder [Kellet B J and Lange F F, 1983].

6.3. Influence of pulsed electric current

While the preceding discussions on particle size and agglomeration explains the multi-step sintering and partly explains the lowering of the activation energy, the effect of an electric field and high currents during sintering and their implications on sintering are discussed in this section. A thin recrystallized region between the WC particles can result by overheating at the neck regions – a characteristic of the SPS method. In the actual experiment, the external current flowing through the sample was found to increase continuously as the compact densified. The small particle size and the high current (~ 700 A at peak densification) can be expected to induce very high current densities on the particle surface. An approximate calculation of the local temperature gradient between the interior and surface of a nano particle can be carried out using a recent model of SPS proposed by Olevsky and Froyen [Eugene Olevsky and Froyen, 2009]. In their model of heat conduction in SPS, the local temperature gradient, without considering heat loss is given by:

$$\nabla T = \frac{1}{G+r_p}\sqrt{\frac{E^2 \Delta t \lambda_e T_0}{2nC}} \tag{12}$$

where, G is the grain size, r_p is the pore radius, C is the specific heat capacity, T_0 is the temperature from which sintering is assumed to start (873 K, in this case), E is the electric field (V/m), λ_e is the electrical conductivity, Δt is the total (ON+OFF) pulse sequence duration and n is the number of pulses required to reach the desired temperature. When applied to oxide ceramics with low conductivity like Al_2O_3, local temperature gradients of the order of 10^6 K/m were determined during SPS [Eugene Olevsky and Froyen, 2009].. In our experiments, we used an ON/OFF pulse ratio of 12/2 which corresponds to 39.6 ms ON

time and 6.6 ms OFF time. The ON pulse comprises twelve 3.3 ms pulses. Other approximate values were also plugged in: $G \approx 100$ nm, $r_p \approx 50$ nm, $\Delta t = 46.2$ ms, $n = 120220$, $E \approx 1000$ V/m. The values of C and λ_e were obtained from the literature: $C_{1300K} \approx 0.0175$ J/K/m^3 [Andon et al, 1975]. For a sample with residual porosity P, the heat capacity is given by $C=(1-P)C_{1300K}$ [Eugene Olevsky and Froyen, 2009, Yann Aman *et al*, 2011]. Since data on the electrical resistivity of WC at high temperatures were unavailable, with a knowledge of the room temperature resistivity of WC ($\rho_{300K} \approx 20$ μΩ·m) and the temperature coefficient of resistivity $\alpha \approx 4500$ /K [Grebenkina and Denbnovetskaya, 1968], a linear approximation was applied from 300 K to the temperature of interest (1300 K) using the relation $\rho=\rho_{300K}(1+\alpha\Delta T)$. This approximation, although slightly in error, may yield a variation of one order of magnitude in the final result. The electrical conductivity ($\lambda_e = 1/\rho$) of a sample with residual porosity, P was calculated as $\lambda_e(P,T) = \lambda_e(0,T)[(1-P)/(1+2P)]$ [Eugene Olevsky and Froyen, 2009]. Using these values, $\nabla T \approx 60 \times 10^6$ K/m. Owing to these large gradients, a plasma is more likely to form at the neck area. However, the temperature can be rapidly conducted over the particle surfaces leading to surface melting in a zone of 5-10 nm at the periphery of the grains as observed near the neck of the sintered particles. These regions can then enhance sintering by reducing inter-granular friction leading to more compact packing (densification by particle rearrangement) and provide easy routes for GB diffusion. At higher temperatures or in densely compacted regions, the term, 'grains' is more appropriate than, 'particles'. It was observed that such regions where the microstructure can be described as 'grains', are not surrounded by the recrystallized phase. While the actual observation of a GB phase during SPS of WC has not been reported yet, certain recent investigations by Demiriskyi and co-workers [Demirskyi D et al, 2012] on micrometre sized spherical balls of WC did reveal anomalous diffusion at the inter-particle neck regions. The group conducted some fundamental studies to understand the sintering mechanism in WC during SPS, conventional sintering and Microwave sintering. They measured both the linear shrinkage during the initial stage and also the neck growth rate (by SEM observations). Using the experimentally observed neck growth rate, they calculated the diffusion coefficient and arrived at the surprising result that the diffusion coefficient during SPS was *orders of magnitude higher* than during conventional sintering. This anomalous behaviour was attributed to a highly active surface and recrystallization at the neck region was clearly observed by SEM. Another recent report is from the group of Guyot and co-workers [Guyot P *et al*, 2012], who demonstrated micro welding at inter-particle areas of micron-sized Cu powders. They attribute this to the inductive coupling of the electromagnetic field leading to a decrease in electrical resistivity of the powders by several orders of magnitude (the *Branly effect*). These recent reports clearly suggest that particle overheating can lead to a GB complexion [Jian Luo, 2008, Shen Dillon *et al*, 2009] particularly during the initial stages of SPS.

Our observations of the low temperature sintered samples clearly show that the local field-induced temperature gradients can cause spontaneous melting and welding near the neck regions at temperatures as low as 1323 K. While the process of equilibrium melting (i.e., melting WC particles by slow heating to their melting point) may be expected to increase the activation energy for sintering (component of ΔH arising from the phase transformation of solid to liquid), this surface melting that is expected to occur in SPS is a totally non-equilibrium melting phenomenon which occurs rapidly. As Chaim [Rachman Chaim, 2007]

and Chaim and Reinharz [Chaim R and Reinharz Bar-Hama, 2010] have suggested, this GB complexion leads to a plastically softened surface layer which can activate rapid atomic diffusion and promote particle rearrangement and creep leading to very low activation energies during sintering. At high temperatures, the 'particle' identity is lost and grain growth rate also increases. The thickness of the recrystallized layer decreases in comparison to the grain size, although the GB is still an active diffusion route until complete densification is achieved. This idea is consistent with our observed kinetic results and the microstructure.

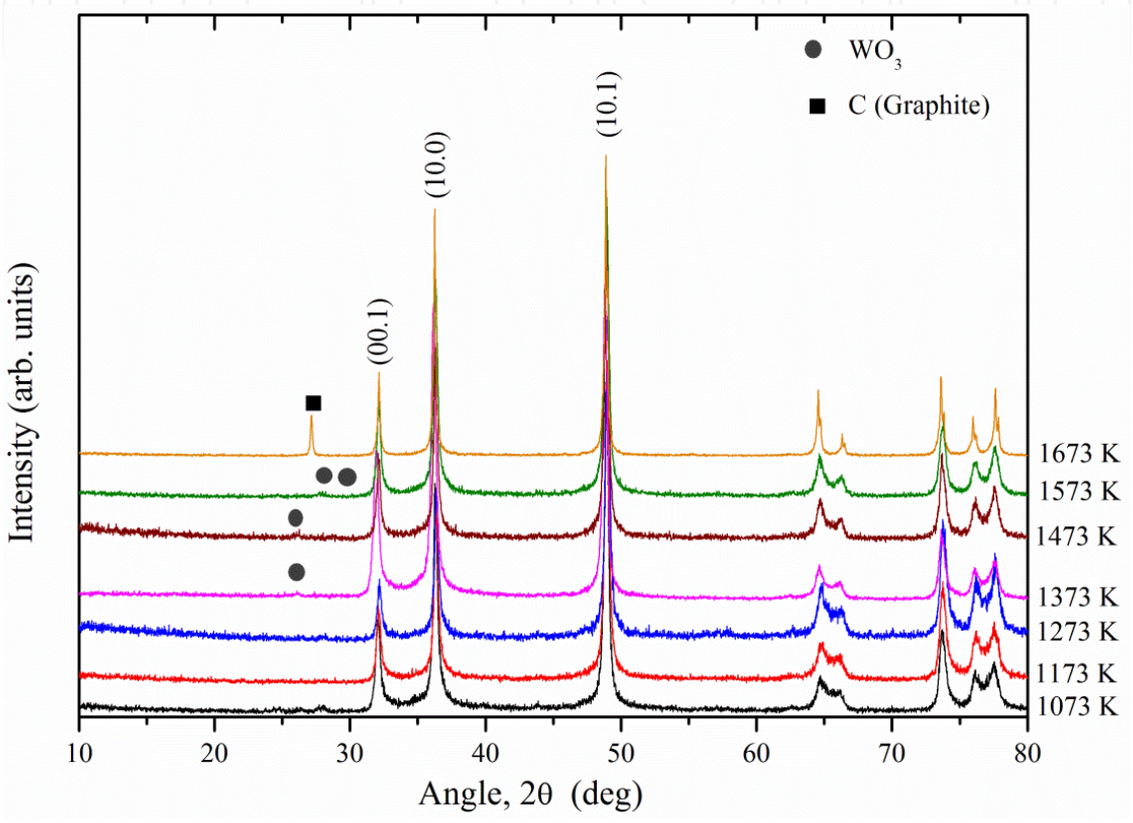


Figure 23. XRD of the samples interrupted at different temperatures. The WO_3 phase is seen at almost all low temperatures, while the final compact only shows WC and graphite. All the primary peaks are from the WC phase.

7. Conclusions

The SPS behaviour of *n*-WC appears to be a complex process involving size effects, field effects, chemical reactions and anomalously rapid diffusion. Experimental observations described in this work show evidence of planar defects, possible GB reconstruction and agglomeration that can contribute to the lowering of the sintering activation energy. In our analysis and from the current volume of literature cited to support our view, it is clear that the fundamental aspects of sintering pertaining to nano particles particularly in the presence of an electromagnetic field can be largely different, for which an exact theory is yet to be developed. A few significant results of this work are given below to summarize our findings:

1. The presence of excessive planar defects in the powder suggests that the quality of the nano powder is crucial for determining the sintering kinetics. In addition to defects, powder agglomeration controls sintering for most of the temperature range.
2. The low activation energies observed encourage efforts to consolidate nano powders to full density. However, not all temperatures are suitable for the sintering process, as agglomerates strongly impede densification at low temperatures. In those temperature ranges where agglomerates retard shrinkage, active surface diffusion and particle rearrangement acts to increase the compact density.
3. While at low temperatures the current assisted, over-heated surface is most likely the active diffusion route, at higher temperatures, grain growth acts to reduce the retarding effect of agglomerates leading to enhanced sintering.
4. The net sintering rate in the *n*-WC powder can be equated to the sum of three factors: $(\dot{\rho})_{total} = (\dot{\rho})_{defects} + (\dot{\rho})_{SD-PR} + (\dot{\rho})_{GB}$.

While the sintering mechanisms detailed in this work are not conclusive, it can be regarded as a pointer for furthering our understanding of the sintering behaviour of *n*-WC. The experimental observations do suggest that alternate, yet novel mechanisms are active during the SPS of *n*-WC, and certain factors that can be responsible have been discussed at length. However, a consistent theory of nano sintering specific to *n*-WC is still necessary. Such a description should therefore include the effects of GB plasticity and creeping induced by dislocation climb and glide in addition to the surface overheating phenomenon in nano materials during SPS. These points are motivated by the fact that even in a brittle material like WC, plasticity effects can be significantly enhanced as the 'GB phase' fraction increases.

Author details

A.K. Nanda Kumar
Dept. of Materials Science and Engineering, Case Western Reserve University, Cleveland, Ohio,
USACentre for Advanced Research of Energy and Materials, Faculty of Engineering, Hokkaido University, Sapporo, Japan

Kazuya Kurokawa
Centre for Advanced Research of Energy and Materials, Faculty of Engineering, Hokkaido University, Sapporo, Japan

Acknowledgement

This work was carried out while AKNK was a foreign researcher at Hokkaido University, Japan. The project was partly funded by the Ohtaseiki Co., Ltd., Japan. AKNK also wishes to express his deep sense of gratitude to Prof. K Kurokawa, for having introduced him to this work and for providing financial support during his stay in Japan. Profs. A Yamauchi and N

Sakaguchi are also gratefully acknowledged for their timely help with the SPS and TEM work and also for many discussions during the course of this work.

8. References

[1] Agrawal D, Cheng J, Seegopaul P, Gao L, Grain growth control in microwave sintering of ultrafine WC-Co composite powder compacts, Powder Metall., 43 (2000) 15-16.

[2] Andon R J L, Martin J F, Mills K C and Jenkins T R, Heat capacity and entropy of tungsten carbide, I. Chem. Thermodynamics, 7 (1975) 1079-1084.

[3] Andrievky R A and Spivak I I, Strength of high melting point compounds - A Companion, Metallurgy, Moscow, (1983) [in Russian].

[4] Ashby M F, A first report on sintering diagrams, Acta Metall., 22 (1974) 275-289.

[5] Bacmann J J, Cizeron G, Dorn Method in the study of initial phase of uranium dioxide sintering, J. Am. Ceram. Soc., 51 (1968) 209–212.

[6] Bartha L, Atato P, Toth A L, Porat R, Berger S and Rosen A, Investigation of hip-sintering of nanocrystalline WC/Co powder, J. Adv. Mater., 32 (2000) 23-26.

[7] Beere W, The second stage sintering kinetics of powder compacts, Acta Metall., 23 (1975) 139-145.

[8] Bernard-Granger G and Guizard C, Spark plasma sintering of a commercially available granulated Zirconia powder I. Sintering path and hypotheses about the mechanism(s) controlling densification, Acta Mater., 55 (2007) 3493-3504.

[9] Breval E, Cheng J P, Agrawal D K , Gigl P, Dennis M and Roy R, Comparison between microwave and conventional sintering of WC/Co composites, Mat. Sci. Eng. A, 391 (2005) 285 -295.

[10] Buhsmer C P and Crayton P H, Carbon self-diffusion in tungsten carbide, J. Mater. Sci., 6 (1971) 981–988.

[11] Byung-Kwon Yoon, Bo-Ah Lee, Suk-Joong L. Kang, Growth behavior of rounded (Ti,W)C and faceted WC grains in a Co matrix during liquid phase sintering, Acta Mater., 53 (2005) 4677.

[12] Chaim R, Reinharz Bar-Hama O, Densification of nanocrystalline NiO ceramics by spark plasma sintering, Mat. Sci. Eng. A, 527 (2010) 462–468.

[13] Coble R L, Initial sintering of alumina and hematite, J. Am. Ceram. Soc., 41 (1958) 55–62.

[14] Coble R L, Sintering crystalline solids. I. Intermediate and final state diffusion models, J. Appl. Phys., 32 (1961a) 787–792.

[15] Coble R L, Sintering crystalline solids. II. Experimental test of diffusion models in powder compacts, J. Appl. Phys. 32 (1961b) 793–799.

[16] Cremer G D, (1944) *US Patent* No. 2,355,954.

[17] Demirskyi D, Hanna Borodianska, Dinesh Agrawal, Andrey Ragulya, Yoshio Sakka and Oleg Vasylkiv, Peculiarities of the neck growth process during initial stage of spark-plasma, microwave and conventional sintering of WC spheres, J. Alloy. Compd., 523 (2012) 1– 10.

[18] Di Yang, Rishi Raj and Hans Conrad, Enhanced sintering rate of zirconia (3Y-TZP) through the effect of a weak dc electric field on grain growth, J. Am. Ceram. Soc., 93 (2010) 2935–2937.

[19] Dominguez O and Bigot J, Material transport mechanisms and activation energy in nanometric Fe powders based on sintering experiments, Nanostruct. Mater., 6 (1995) 877-880.

[20] Duran P, Villegas M, Capel F, Recio P and Moure C, Low-temperature sintering and microstructural development of nanocrystalline Y-TZP powders. J. Eur. Ceram. Soc., 16 (1996) 945-952.

[21] Eugene A. Olevsky, Ludo Froyen, Impact of thermal diffusion on densification during SPS, J. Am. Ceram. Soc., 92 [S1] (2009) S122–S132.

[22] Giovanni Maizza, Salvatore Grasso, Yoshio Sakka, Tetsuji Noda and Osamu Ohashi, Relation between microstructure, properties and spark plasma sintering (SPS) parameters of pure ultrafine WC powder, Sci. Tech. Adv. Mater., 8 (2007) 644–654.

[23] Goren-Muginstein G R, Berger S and Rosen A, Sintering study of nanocrystalline WC powders, Nanostruct. Mater. 10 (1998) 795–804.

[24] Grebenkina V G and Denbnovetskaya E N, Temperature coefficient of electrical resistivity of some complex metal carbides, Translated from Poroshkovaya Metalturgiya (*in Russian*), 63 (1968) 34-36.

[25] Gupta V K , Dang-Hyok Yoon, Harry M. Meyer III and Jian Luo, Thin intergranular films and solid-state activated sintering in nickel-doped tungsten, Acta Mater., 55 (2007) 3131–3142.

[26] Gurland J, Application of dihedral angle measurements to the microstructure of cemented carbides WC–Co, Metallography, 10 (1977) 461–468.

[27] Guyot P, Rat V, Coudert J F, Jay F, Maitre A and Pradeilles N, Does the Branly effect occur in spark plasma sintering?, J. Phys. D: Appl. Phys. 45 (2012) 092001-092005.

[28] Hulbert D M, Anders A, Andersson J, Lavernia E J and Mukherjee A K , A discussion on the absence of plasma in spark plasma sintering, Scripta Mater., 60 (2009) 835–838.

[29] Hulbert D M, Anders A, Dudina D V, Andersson J, Jiang D, Unuvar C, Anselmi-Tamburini U, Lavernia E J and Mukherjee A K, The absence of plasma in 'spark plasma sintering', J. Appl. Phys., 104 (2008) 033305.

[30] Itatani K, Itoh A, Howell F S, Kishioka A and Kinoshita M, Densification and microstructure development during the sintering of sub-rnicrometre magnesium oxide articles prepared by a vapour-phase oxidation process, J. Mater. Sci., 28 (1993) 719-728.

[31] Jian Luo, Liquid-like interface complexion: From activated sintering to grain boundary diagrams, Curr. Opin. Solid St. Mater. Sci., 12 (2008) 81–88.

[32] Jiang X X, Huang Dong-Shen and Weng Lu Quian, Sintering characteristics of microfine zirconia powder, J. Mater. Sci., 29 (1994) 121-124.

[33] Johnson D L and Cutler I B, Diffusion sintering: I, Initial stage sintering models and their application to shrinkage of powder compacts, J. Amer. Ceram. Soc., 46 (1963a) 541-545.

[34] Johnson D L and Cutler I B, Diffusion sintering: II, Initial sintering kinetics of Alumina, J. Amer. Ceram. Soc., 46 (1963b) 545-549.

[35] Kellett B J and Lange F F, Thermodynamics of densification. I. Sintering of simple particle arrays, equilibrium configurations, pore stability and shrinkage, J. Am. Ceram. Soc., 72 (1989) 725–741.

[36] Kim H C, Oh D Y and Shon I J, Sintering of nanophase WC-15 Vol.% Co hard metals by rapid sintering process, Int. J. Refract. Met. Hard Mater., 22 (2004) 197 – 203.

[37] Kinemuchi Y and Watari K, Dilatometer analysis of sintering behavior of nano-CeO_2 particles, J. Eur. Ceram. Soc., 28 (2008) 2019–2024.

[38] Kingery W D and Berg M, Study of initial stages of sintering solids by viscous flow, evaporation-condensation and self-diffusion, J. Appl. Phys., 26 (1955) 1205-1212.

[39] Kingery W D, Bowen H K and Uhlmann D R, Introduction to Ceramics, second ed., John Wiley and Sons, New York, 1975.

[40] Knorr P, Nam J G and Lee J S, Sintering behaviour of nano crystalline γ-NiFe powders, Metall. Mater. Trans. A, 31A (2000) 506-510.

[41] Kumar A K N, Watabe M, Yamauchi A, Kobayashi A and Kurokawa K, Spark plasma sintering of binderless n-WC and n-WC-X (X=Nb, Re, Ta, Ti, B, Si), Trans. JWRI, 39 (2010) 47-56.

[42] Lanfredi S, Dessemond L and Martins Rodrigues A C, Dense ceramics of $NaNbO_3$ produced from powders prepared by a new chemical route, J. Eur. Ceram. Soc., 20 (2000) 983-990.

[43] Lange F F, Sinterability of agglomerated powders, J. Am. Ceram. Soc., 67 (1984) 83–89.

[44] Li J G and Sun X, Synthesis and sintering behaviour of a nano crystalline α-alumina powder, Acta mater., 48 (2000) 3103-3112.

[45] Li T, Li Q, Lu L, Fuh J Y H and Yu P C, Abnormal grain growth of WC with small amount of cobalt, Philos. Mag. A, 87 (2007) 5657-5671.

[46] Luca Girardini, Mario Zadra, Francesco Casari and Alberto Molinari, SPS, binderless WC powders and the problem of subcarbide, Met. Powder Rep., (2008) 18-22.

[47] Munir Z A, Anselmi-Tamburini U and Ohyanagi M, The effect of electric field and pressure on the synthesis and consolidation of materials: A review of the spark plasma sintering method, J. Mater. Sci., 41 (2006) 763–777.

[48] Nabarro F R N, Bartolucci Luyckx S and Waghmare U V, Slip in tungsten monocarbide II. A first-principles study, Mater. Sci. Eng. A, 483-484 (2008) 9-12.

[49] Nobre M A L, Longo E, Leite E R and Varela J A, Synthesis and sintering of ultrafine NaNbO powder by use of polymeric precursors. Mater. Lett., 28 (1996) 215-220.

[50] Panda P C, Mobley W M and Raj R, Effect of the Heating Rate on the Relative Rates of Sintering and Crystallization in Glass, J. Am. Ceram. Soc., 72 (1989) 2361-2364.

[51] Rachman Chaim, Densification mechanisms in spark plasma sintering of nanocrystalline ceramics, Mater. Sci. Eng. A, 443 (2007) 25–32.

[52] Rahman M N, Ceramic Processing and Sintering, 2nd ed., Marcel Dekker, New York, (2003).

[53] Raj R and Bordia R K, Sintering behavior of bi-modal powder compacts, Acta Metall., 32 (1984) 1003-1019.

[54] Salvatore Grasso, Yoshio Sakka and Giovanni Maizza, Electric current activated/assisted sintering (*ECAS*): a review of patents 1906–2008, Sci. Technol. Adv. Mater., 10 (2009) 053001.

[55] Shen J. Dillon, Martin P. Harmer, and Jian Luo, Grain Boundary Complexions in Ceramics and Metals: An Overview, JOM, 61 (2009) 38-44.

[56] Shi, J. L., Lin, Z. X., Qian, W. J. and Yen, T. S., Characterization of agglomerate strength of coprecipitated superfine zirconia powders. J. Eur. Ceram. Soc., 13 (1994) 265-273.

[57] Swinkels F B and Ashby M F, A second report on sintering diagrams, Acta Metall., 29 (1980) 259-281.

[58] Theunissen G S A M, Winnubst A J A and Burggraaf A J, Sintering kinetics and microstructure of nanoscale Y-TZP ceramics, J. Eur. Ceram. Soc., 11 (1993) 315-324.

[59] Tokita M, Mechanism of Spark Plasma Sintering, in Proceedings of the International Symposium on Microwave, Plasma and Thermomechanical Processing of Advanced Materials, ed. S. Miyake and M. Samandi. JWRI, Osaka University, Japan (1997) 69–76.

[60] Tokita M, Suzuki S and Nakagawa K (2007) *Euro. Patent* No. EP1839782.

[61] Victor Zamoraa, Angel L. Ortiz, Fernando Guiberteau and Mats Nygren, Spark-plasma sintering of ZrB2 ultra-high-temperature ceramics at lower temperature via nanoscale crystal refinement, J. Eur. Ceram. Soc., 32 (2012) 2529–2536.

[62] Wang J and Raj R, Estimate of the activation energies for boundary diffusion from rate controlled sintering of pure alumina and alumina doped with zirconia and titania, J. Am. Ceram. Soc., 73 (1990) 1172-1175.

[63] Wenming Zeng, Lian Gao, Linhua Gui and Jinkun Guo, Sintering kinetics of α-Al_2O_3 powder, Ceram. Int., 25 (1999) 723-726.

[64] Yann Aman, Vincent Garnier and Elisabeth Djurado, Spark plasma sintering kinetics of pure α-Alumina, J. Am. Ceram. Soc., 94 (2011) 2825–2833.
[65] Young W S and Cutler I B, Initial sintering with constant rates of heating, J. Am. Ceram. Soc., 53 (1970) 659–663.

IntechOpen

IntechOpen